Fat Subtraction Protocol for Wide-Angle X-ray Scatter Analysis of Breast Biopsies

by

Nancy McDonald

A thesis submitted in partial fulfillment
of the requirements for the degree of
Master of Science (MSc) in Physics

The Faculty of Graduate Studies
Laurentian University
Sudbury, Ontario, Canada

THESIS DEFENCE COMMITTEE/COMITÉ DE SOUTENANCE DE THÈSE
Laurentian Université/Université Laurentienne
Faculty of Graduate Studies/Faculté des études supérieures

Title of Thesis Titre de la thèse	Fat Subtraction Protocol for Wide-Angle X-ray Scatter Analysis of Breast Biopsies
Name of Candidate Nom du candidat	McDonald, Nancy
Degree Diplôme	Master of Science
Department/Program Département/Programme	Physics
Date of Defence Date de la soutenance	March 21, 2016 2:30 PM

APPROVED/APPROUVÉ

Thesis Examiners/Examinateurs de thèse:

Dr. Eduardo Galiano-Riveros
(Supervisor/Directeur(trice) de thèse)

Dr. Ubi Wichoski
(Committee member/Membre du comité)

Dr. Robert Speller
(External Examiner/Examinateur externe)

Approved for the Faculty of Graduate Studies
Approuvé pour la Faculté des études supérieures
Dr. David Lesbarrères
Monsieur David Lesbarrères
Acting Dean, Faculty of Graduate Studies
Doyen intérimaire, Faculté des études supérieures

ACCESSIBILITY CLAUSE AND PERMISSION TO USE

THESIS DEFENCE COMMITTEE/COMITÉ DE SOUTENANCE DE THÈSE
Laurentian Université/Université Laurentienne
Faculty of Graduate Studies/Faculté des études supérieures

Title of Thesis Titre de la thèse	Fat Subtraction Protocol for Wide-Angle X-ray Scatter Analysis of Breast Biopsies
Name of Candidate Nom du candidat	McDonald, Nancy
Degree Diplôme	Master of Science
Department/Program Département/Programme	Physics
Date of Defence Date de la soutenance	March 21, 2016 2:30 PM

APPROVED/APPROUVÉ

Thesis Examiners/Examinateurs de thèse:

Dr. Eduardo Galiano-Riveros
(Supervisor/Directeur(trice) de thèse)

Dr. Ubi Wichoski
(Committee member/Membre du comité)

Dr. Robert Speller
(External Examiner/Examinateur externe)

Approved for the Faculty of Graduate Studies
Approuvé pour la Faculté des études supérieures
Dr. David Lesbarrères
Monsieur David Lesbarrères
Acting Dean, Faculty of Graduate Studies
Doyen intérimaire, Faculté des études supérieures

ACCESSIBILITY CLAUSE AND PERMISSION TO USE

Abstract

Breast cancer detection often involves the use of mammography to locate suspicious lesions followed by extraction of some tissue within the lesion via a biopsy procedure. The gold standard method for determining whether the extracted tissue is malignant or benign is an histological analysis. However, complimentary x ray methods such as x-ray fluorescence (XRF), small-angle x-ray scatter (SAXS) and wide-angle x-ray scatter (WAXS) have been investigated by various groups. The focus of this dissertation was to develop a WAXS fat subtraction protocol for the WAXS analysis of breast tissue biopsies. The WAXS signals of breast tissue could become an additional source of diagnostic information.

Healthy breast tissue is composed of fat and fibroglandular (fibrous) tissue. Comparisons of the WAXS signals of fibroglandular and cancerous tissue are difficult because biopsies of either type usually contain some fat tissue. The ability to look at WAXS signals independent of the fat contribution could be informative. The goal of this work was to validate a WAXS fat subtraction protocol using an animal tissue sample consisting of a mixture of fat and fibrous tissue. The differential linear scattering coefficient $d\mu_s/d\Omega$ of a region of interest (ROI) within the sample was measured via energy dispersive x-ray diffraction measurements using a custom built CdTe diffractometer. The mean fractional volume of fat ($\overline{\nu}_{\text{fat}}$) within the ROI was estimated using a digital x ray imaging system. The transfer of the sample from the

WAXS system to the digital system required accurate knowledge of the ROI. The use of $\overline{\nu}_{\text{fat}}$ in a WAXS fat subtraction model then allowed the $d\mu_s/d\Omega$ of fibrous tissue to be estimated. The signals obtained via the subtraction protocol agreed well with the signals obtained using pure tissue samples.

The scattering coefficient $d\mu_s/d\Omega$ is a function of the momentum transfer argument $x = 1/\lambda \sin(\theta/2)$, a variable that combines the dependence of scatter on photon λ and scatter angle θ. Accessing a larger x space could provide more information about the nature of breast tissue. Modifications to the custom built diffractometer were implemented in order to access a larger x space. Specifically, the capability to measure signals at smaller θ and the use of higher kV beams were the outcomes. Preliminary results obtained with water, polymethyl methacrylate, and polycarbonate samples were promising, yet suggested that better collimation is required between the sample and the detector in order to reduce scatter contamination from objects located downstream from the sample.

Acknowledgements

I would like to thank all the staff and students at Laurentian University who have made it possible for me to complete my research. Very special thanks to my supervisors; Dr. Eduardo Galiano-Riveros and Dr. Robert LeClair as well as my committee member Dr. Ubi Wichoski for their guidance and support.

Finally, I want to thank my family and friends. All my parents; Ewa, Stasiu, Wiesia, Doug and Karin. My wonderful siblings Ola, Margaret, Ewelina, Iwona and Beata as well as all their children, husbands etc etc etc. The time spent with you has often been the vacation I needed. To my friends back home for sticking by me through the distance and those in Sudbury for welcoming me. Most important of all I want to acknowledge my husband and best friend, Bryan, for his continued support, humour and above all patience.

Contents

List of Figures

List of Tables

Chapter 1

Introduction

One out of nine women between the ages of 20 and 90 years old are expected to develop breast cancer in Canada. Since 1983 death attributed to the disease has decreased by 42% due to advances in technology allowing for faster diagnosis, better treatment and awareness. [43] The diagnosis of suspicious lesions is routinely done via removal of tissue and its subsequent analysis via histology. The tissue samples extracted undergo an histology analysis by a pathologist for determining whether malignancy is present. If present then the type and stage of the malignancy [36] is determined. Only certain slices of a tissue sample are analyzed under the microscope and therefore cancers could potentially be missed if the proper slice is not studied. Complimentary methods to diagnose breast cancer in biopsies could prove useful to the medical community.

Raman spectroscopy measures the inelastic scattering of light from tissue caused by vibration and rotation of molecules. The recorded spectrum provides unique infor-

mation about the material interrogated. Several groups have been investigating the validity of Raman spectroscopy with applications to breast cancer diagnosis. [5, 4] Abramczyk *et al.* [1]conducted a statistically significant study in 2009. 1100 spectra from 99 patients were analysed to distinguish between normal, malignant and benign breast tissue. Two Principle Component Analysis (PCA) criteria were used; PC1–characteristic Raman peaks and PC2–autofluorescence. The former resulted in a 73% sensitivity for malignant tissue, 62% for the benign tissue as well as a specificity of 83% for normal tissue. The latter criteria resulted in sensitivity of 55% for the malignant tissue and 32% for benign tissue. The combination of both components provided good distinction between healthy and diseased tissue. Results were also consistent with cancer studies that concluded women with higher breast density are more likely to develop cancer as opposed to those with fatty breast tissue.

In this work some Raman spectroscopy measurements on animal tissue were conducted at the Central Analytical Facility at Laurentian University. However, due to the small penetration depth of lasers the method was abandoned in favour of wide angle x-ray scatter (WAXS) which is capable of probing an entire biopsy volume of tissue. The use of wide-angle x-ray scatter (WAXS) signals to diagnose cancer in breast biopsies have been investigated by various researchers. [11, 2, 49, 41, 46, 35, 14, 40, 9, 26, 39, 8, 38, 21, 10]

Farquharson *et al.* [11] recently reported results of combining x-ray fluorescence (XRF) and WAXS for the classification of breast specimens. The former provided

quantification of concentrations of K, Ca, Zn, Fe, Cu, Br and Rb whereas the latter provided their coherent scattering properties. The data were incorporated into a multivariate model [i.e. principal component analysis and soft independent modelling of class analogies (SIMCA)]. [40] Their findings were mapped to histological analysis of the samples. They suggest that their model can potentially be used to classify a small tissue sample as benign or malignant.

Elshemy *et al.* [49] measured the scatter signals at angles ranging from 4° to 70° (increments of $\Delta\theta = 0.5°$) of 36 breast tissue samples using an x-ray diffractometer consisting of a Cu anode x-ray tube operating at 40 kV. The Cu Kα = 8.047 keV scattered photons were selected by a graphite monochromator and detected by a sodium iodide crystal. Scatter profiles were peak normalized and it was concluded that characterization parameters (e.g. full width half maximum (FWHM), ratios of scatter intensities, areas under the curve) could be useful for diagnostic evaluations. The scatter profiles were given as a function of the momentum transfer variable $x = 1/\lambda \sin(\theta/2)$ given in units of inverse nanometers. For example, FWHM mean values of 0.50 ± 0.16 nm^{-1} and 1.18 ± 0.28 nm^{-1} were found for respectively healthy and malignant tissue.

Changizi *et al.* [46] measured diffraction profiles of 131 breast biopsies using a HPGe detector positioned at $\theta = 6°$. A tungsten target x-ray tube operating at 55 kV was used. Differences in the peak positions were observed for normal, carcinoma and benign tissue. The peak heights found for carcinoma were located at 1.55 $\pm$

0.04 nm^{-1}, 1.73 $\pm$ 0.06 nm^{-1}, and 1.85 $\pm$ 0.05 nm^{-1}, while adipose/fibroglandular mixtures yielded peaks at 1.15 $\pm$ 0.06 nm^{-1} and 1.4 $\pm$ 0.05 nm^{-1}. The differences between fibrocystic changes (e.g. non-malignant breast lumps) and carcinoma were insignificant and the different types of carcinomas could not be distinguished (e.g. ductal carcinoma, lobular carcinoma).

Oliveira *et al.* [35] investigated the use of a powder diffractometer consisting of an x-ray tube with a Cu anode, a graphite monochromator selecting Kα = 8.047 keV photons and a sodium iodide detector. Scatter signals from $\theta = 5^\circ$ to 150° ($\Delta\theta = (1/3)^\circ$) were measured for 40 samples initially identified with histology. The scatter profiles for water were measured and agreed with measurements by Morin *et al.* [33] Normal glandular tissue yielded a peak at 1.7 nm^{-1}. The diffraction patterns for glandular, benign and malignant tissue showed similar shapes but differed in peak heights. A discriminant analysis was used to classify biopsies. A sensitivity of 95.6% and a specificity of 82.3% were found for differentiating normal fibroglandular and malignant tissue.

Ryan *et al.* [40] used an energy dispersive x-ray system (W anode tube operating at 80 kV with a HPGe detector) to analyse 39 breast tissue samples. The samples were classified by histology as adipose, fibroadenoma, fibrocystic change, malignant, and normal fibrous tissue. The electron densities were estimated from Compton scatter measurements ($\theta = 30^\circ$, 57.97 keV Kα2 radiation). The x-ray diffraction signatures were acquired at $\theta = 7.5^\circ$ with a measurement time of 1 hr for each sample. The

data were used to classify the tissue via SIMCA methods with a sensitivity of 54% and specificity of 100%.

WAXS applications for diagnosing breast cancer in biopsies have, however, not yet made the clinical scene. Differences between the WAXS signals of cancer and fibroglandular tissue have been reported, yet consensus has not been achieved. A difficulty that arises when trying to measure the scatter signals of cancer and fibroglandular tissue is the possible presence of fatty tissue. In this work, a WAXS fat subtraction protocol is presented which can be used with breast tissue so that the differential linear scattering coefficient $d\mu_s/d\Omega$ of cancer and fibrous can be compared independent of fat tissue effects. For validation purposes, animal tissue was used instead of actual breast tissue. A method to estimate the mean fractional volume of fat $\overline{\nu}_{\text{fat}}$ within a region of interest (ROI) of an animal tissue sample for WAXS analysis was devised. The use of $\overline{\nu}_{\text{fat}}$ in a WAXS fat subtraction model, partially validated in a previous work [45] and further validated in this work, was used to estimate $d\mu_s/d\Omega$ of the non-fat tissue within the ROI.

Chapter 2

Physics of X Rays

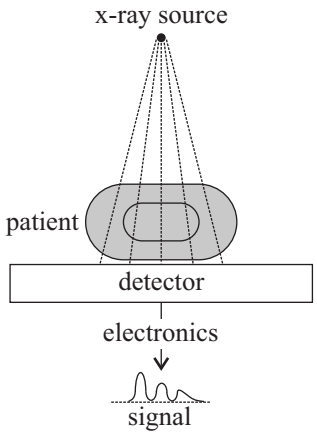

Figure 2.1: Typical diagnostic x-ray set up.

The field of x-ray diagnostics is concerned on the use of x rays to diagnose disease in the human body. Figure 2.1 shows a schematic of a patient being partially irradiated by x-rays. The goal of diagnostics is to capture the x ray field transmitted through the patient with a detector and analyze the signals to determine whether cancer is present. In this chapter I describe briefly how x rays are produced, interact with

matter and are detected. The descriptions are focused only on the areas of interest to this work which involve the interrogation of tissue specimens with polychromatic x rays.

2.1 X-ray Production

In our lab, the production of x-rays is achieved through the use of a stationary anode x-ray tube. Figure 2.2 shows a typical schematic. The cathode is made out of a metal filament and is generally referred to as the negative electrode. Electrons form a cloud when the filament is heated via an applied current then accelerated via a high voltage difference towards the anode. The anode metal is tungsten. Collisions of the electrons with the anode yield two types of radiation; Brehmsstralung and characteristic radiation.

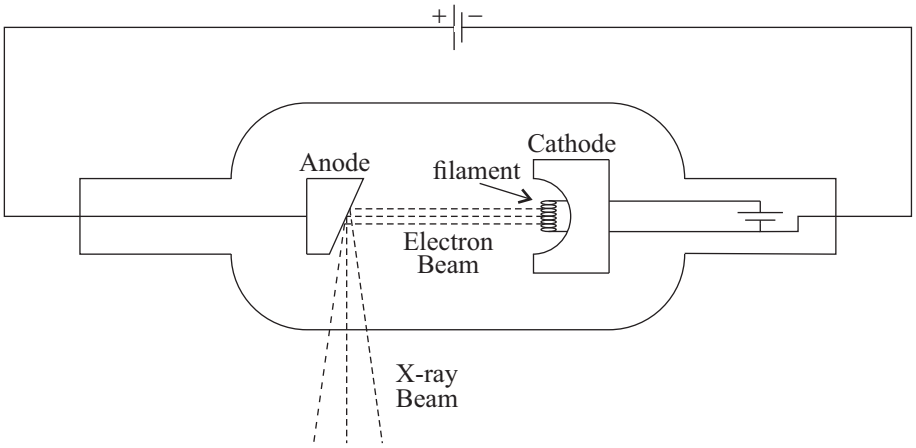

Figure 2.2: X-ray tube schematic.

Bremsstrahlung or "braking radiation" occurs when an electron is decelerated by

the electric field produced by the nucleus of an atom. Some of the kinetic energy loss by the electron during the deceleration is converted into photons while the remaining energy simply heats up the anode material. A continuous spectrum of photon energies is obtained during such processes. Since the photon energy is dependent on the energy of the incoming electron none of the produced radiation can have a higher energy than the kinetic energy of the electron incident on the anode. The maximum energy of a Bremsstrahlung photon is equivalent to the product of the electron charge and the accelerating potential between the anode and cathode.

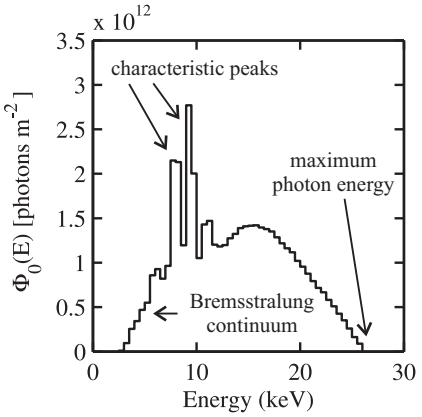

Figure 2.3: Photon fluence produced using a tungsten anode and 26 kV potential.

Characteristic radiation is the result of electrons, incident on the anode, knocking electrons from orbit. The target electrons are ejected from the atom resulting in a hole in the valence shell. If a K-shell electron was knocked out then an L-shell electron can drop to fill the vacancy. In the process an x-ray photon can be released. The energy of the photon is given by $E = EB_K - EB_L$ where EK_B and EL_B are the binding energies of the electron shells. Figure 2.3 shows a x-ray photon fluence spectrum

obtained using a tungsten anode and a potential energy of 26 kV. Highlighted is the Bremsstrahlung continuum as well as the L-fluorescence characteristic x rays.

The x-ray spectrum may be altered by modifying the number of electrons which are accelerated towards the anode. This is done by increasing or decreasing the exposure time(s) or the tube current (mA). The milliampere second (mAs) is the product of the tube current with the exposure time; it is a unit which describes how the x-ray spectrum is scaled by these variables. Intrinsic filtration effects the resultant x-ray spectrum by attenuating some of the x rays produced within the anode. A filter may be used to increase the average energy of the x ray spectrum by attenuating out the low energy x rays. This is also referred to as beam hardening.

2.2 Interaction of X Rays with Matter

2.2.1 Linear Attenuation Coefficient

Consider a beam of x-rays consisting of photons with energy E incident on a material of thickness Δx as shown in Figure 2.4. $N_0(E)$ denotes the number of photons. As the x rays pass through the material some are attenuated through various modes of interaction. The incident x rays that make it through without interacting are called primary photons. Mathematically, the number of primary photons is given by

$$N_p(E) = N_0(E)e^{-\mu(E)\Delta x} \tag{2.1}$$

where $\mu(E)$ is the linear attenuation coefficient in units of cm^{-1}. This coefficient which is a function of E describes the attenuation of x rays and is given by

$$\mu(E) = \mu_{\mathrm{pe}}(E) + \mu_{\mathrm{inc}}(E) + \mu_{\mathrm{coh}}(E) + \mu_{\mathrm{pp}}(E) \tag{2.2}$$

where the subscripts denote photoelectric (pe), incoherent scattering (inc), coherent scattering (coh) and pair production (pp), respectively. Pair production is not observed in the diagnostic x-ray energy range since it does not occur under 1.022 MeV, therefore, will not be discussed. The remaining interactions will be discussed below.

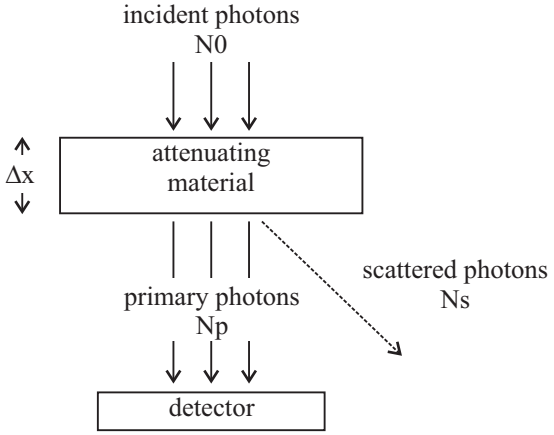

Figure 2.4: Attenuation of x rays by a material.

Photoelectric absorption occurs when a low energy photon is absorbed by an atom. During this interaction a bound electron of the atom is ejected from its orbital shell. The ejected electron is referred to as a photo-electron and its' energy is given by the difference between the energy of the incident photon and the binding energy of the ejected electron. The probability for this process to occur is highest when the

energy of the incident photon is equal to or slightly higher than the binding energy of the electron. The probability is proportional to $\rho Z^3/E^3$ and is generally predominate in an energy range of 10 to 25 keV.

Incoherent scattering also known as Compton or inelastic scattering is a process by which a photon interacts with an outer shell electron (loosely bound). The process results in a scattered photon as well as an ejected electron. The process is mostly independent of Z and instead relies on the electron density of the material, ρ_e. It's occurrence increases from low energy and peaks at $\approx$150 keV then decreases with further increase in energy.

Finally, coherent scattering is better described as a wave phenomenon where the incident oscillating electromagnetic wave causes vibration of the electrons within an atom. The vibration results in the release of x rays of the same energy as the incident x ray. Depending on the arrangements of the atoms, constructive and destructive interferences occur as a function of the scatter angle θ defined as the angle between the incident wave and scattered wave directions. θ is equal to twice the Bragg angle. Coherent scattering is predominant at low energies and rapidly decreases until it is a negligible process above 100 keV.

The linear attenuation coefficient is generally what produces contrast between materials during x ray imaging such as mammography. Breast tissue is composed of fat, fibroglandular tissue and potentially cancer. μ values of breast tissue measured by Johns and Yaffe [19] are shown in Figure 2.5. It can be seen that the signals

of cancer and fibroglandular tissue are very similar. Studying the x ray scattering signals could provide more information about breast tissue.

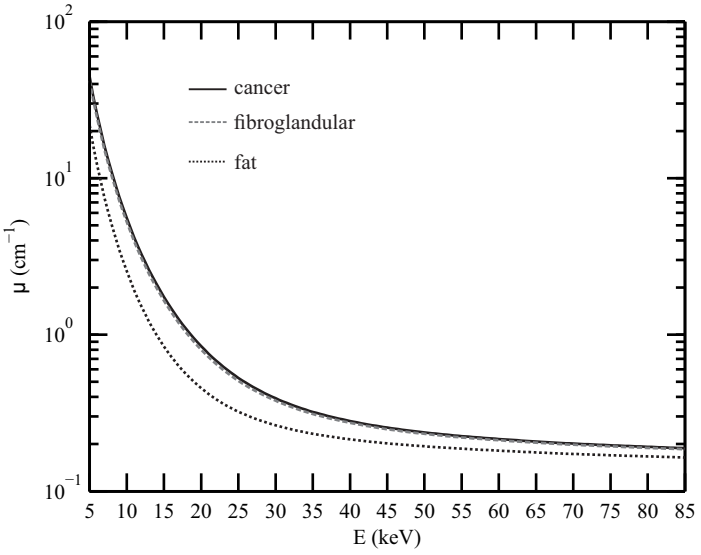

Figure 2.5: Linear attenuation coefficients of breast tissue.[19]

2.2.2 Scattering Coefficients

For a given sample, a quantity referred to as the differential linear scattering coefficient expressed in units of cm^{-1} sr^{-1} is given by

$$\frac{d\mu_{\mathrm{s}}(x)}{d\Omega} = \rho_{\mathrm{e}}\frac{r_0^2}{2}(1+\cos^2\theta)[F^2(x) + F_{\mathrm{KN}}(\lambda,\theta)S(x)], \tag{2.3}$$

where ρ_e = electron density, r_0 = classical electron radius, F and S are the coherent form factor and incoherent scattering function of the sample, and F_{KN} is the Klein-Nishina function. The scatter coefficient $d\mu_{\mathrm{s}}/d\Omega$ describes the attenuation due

to scatter through a given material per unit length per unit solid angle and are a function of $E = hc/\lambda$ and the momentum transfer argument $x = \sin(\theta/2)/\lambda$. The latter variable combines the dependence of scatter on incident photon wavelength λ and scatter angle θ. At low x, it is F (i.e. coherent scatter) which provides most contrast between tissue types but both types of scatter were included in this work.

Figure 2.6 shows for water the ratios of coherent and incoherent cross sections to the total scatter cross section obtained with photons of energy up to 160 keV for (a) $\theta = 6°$ and (b) $\theta = 12°$. As the angle of scatter increases the incoherent scatter

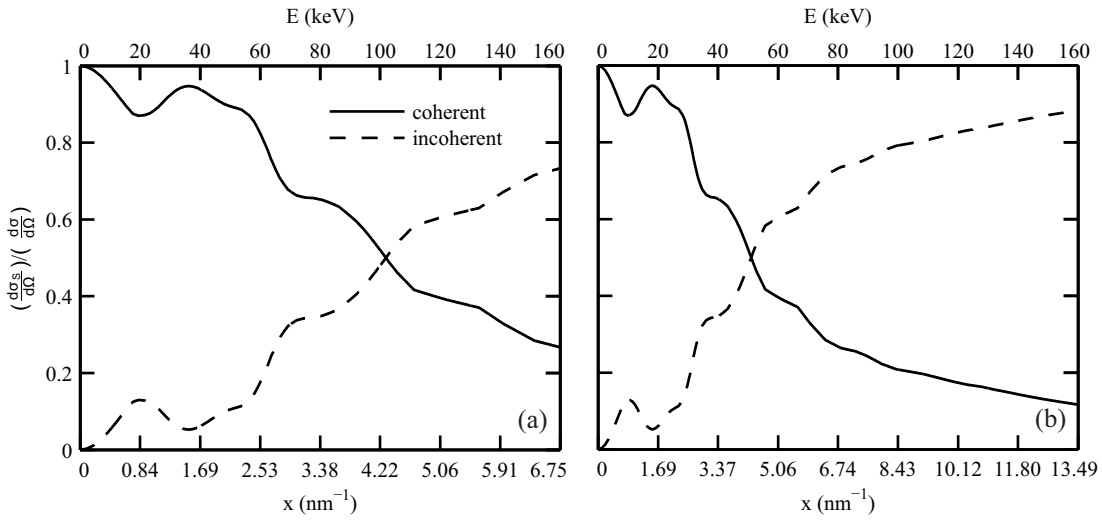

Figure 2.6: Ratios of coherent and incoherent scatter cross sections to the total scatter cross section of water up to 160 keV for (a) $\theta = 6°$ and (b) $\theta = 12°$.

begins to have a larger contribution to the signal for low energy. The line of intersection between the coherent and incoherent scatter in Fig. 2.6 moved closer to a lower energy. As can be seen for $\theta = 6°$ this occured at approximately 100 keV whereas at 50 keV for $\theta = 12°$.

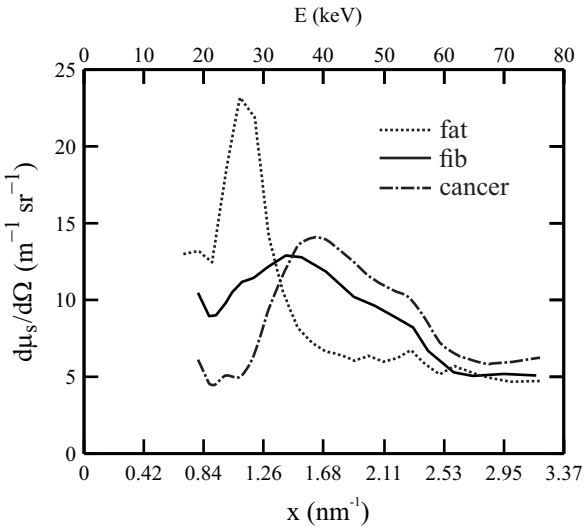

Figure 2.7: Differential linear scattering coefficients of breast tissue.[21]

Kidane et al. [21] conducted a pioneering WAXS work on 100 breast tissue samples. Figure 2.7 shows the differential linear scattering coefficients of breast tissue they acquired via WAXS energy dispersive experiments performed at $\theta = 6°$ using an 80 kV beam and a HPGe detector. The stacking of triacylglycerol molecules in fat cells cause a distinctive peak in $d\mu_s/d\Omega$ at $x = 1.1$ nm^{-1}. Their $d\mu_s/d\Omega$ data for cancer obtained upon removal of the fibrous and fat components were quite different from fibroglandular tissue. Histological analysis of 5 μm sections of the samples was used to determine tissue composition. The use of histology to estimate fat content is questionable because there is no guarantee the composition of the chosen slice is the same throughout the sample. A complementary method of determining the fat content to histology could provide more accurate results. The x-ray method described in Section 3.3 to estimate fat content was a major focus of this work.

2.3 X-Ray Detection

The detection of x rays is done using devices such as radiographic film, energy integrating and photon counting digital detectors. The latter two will be discussed briefly due to their relevance to this work. Both are based on the principal that ionizing radiation generates electron hole pairs upon interacting with a material.

2.3.1 Energy Integrating Detectors

Figure 2.8 shows the principle operation of energy integrating detectors which are commonly used for medical imaging. In this work an MX-20 digital specimen radiography system (Faxitron Bioptics (LLC), Tucson, AZ) was used for the estimation of fat content in biopsy samples. The detector is of the indirect conversion type consisting of a phosphor screen coupled to a CCD camera via a 2:1 fibre optic taper. The x rays transmitted through the sample are absorbed by the phosphor and some of them are converted to visible light photons. A portion of these then travel along the fibre optics to interact with the detector elements (pixels) of the CCD. Within each pixel, some photons are absorbed via the photoelectric effect and thereby generate electric charges which are accumulated during image acquisition. The amount of charge is dictated by the amount of light which in turn depends on the intensity of the x rays incident on the phosphor.

Analog to digital units (ADU) are assigned to pixels; their magnitude is dependent on the amount of charge accumulation. The ADU for a single pixel is the sum of

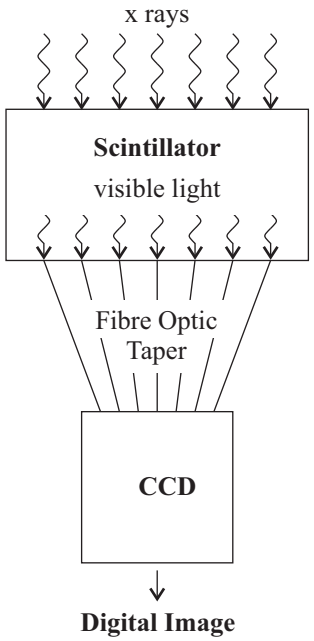

Figure 2.8: Schematic of an indirect conversion digital detector.

energies deposited by photons which traveled through a particular column of tissue for a predetermined amount of time. Figure 2.9 shows a greyscale image of a 3 mm thick piece of Nylon held in a polyethylene container obtained using the MX-20. The contrast seen between different regions is achieved due to variations in thickness and material (density). The darker regions seen are due to less photons depositing energy at the phosphor screen. Images obtained with a CCD need to calibrated for anomalies such as dark current. In our system the MX-20 has a built in calibration protocol.

2.3.2 Photon Counting Detectors

Figure 2.10 shows the set up for a cadmium telluride (CdTe) 25 mm^2 by 1 mm thick crystal (XR-100T-CdTe, Amptek Inc., Bedford MA) photon counting detector

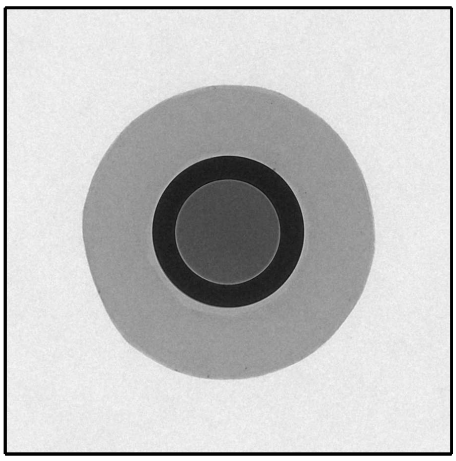

Figure 2.9: CCD, indirect conversion, image of 3 mm thickn Nylon cylinder within a polyethylene holder.

as used in our lab for acquiring WAXS signals. In the diagnostic x ray range (10 to 150 keV) the x rays interact predominantly via the photoelectric effect in the CdTe crystal. Upon absorption with the semiconductor electron hole pairs are created. These charges are attracted towards corresponding positive and negative electrodes and thereby induce a voltage pulse in an external circuit. The role of the charge sensitive preamplifier is to produce an output pulse which has a voltage step proportional to the integral of the current with respect to time. The output pulse is then sent to the shaping amplifier which amplifies the signal, filters out noise and shapes it. Finally, the multichannel analyzer produces the output spectrum; a histogram of the number of pulses which fall into a specific range of amplitudes corresponding to a channel. [3]

Figure 2.11 shows a calibration spectrum measured by the CdTe detector using an Americium (^{241}Am) source. Highlighted are the emission rays of 13.9 keV, 17.8

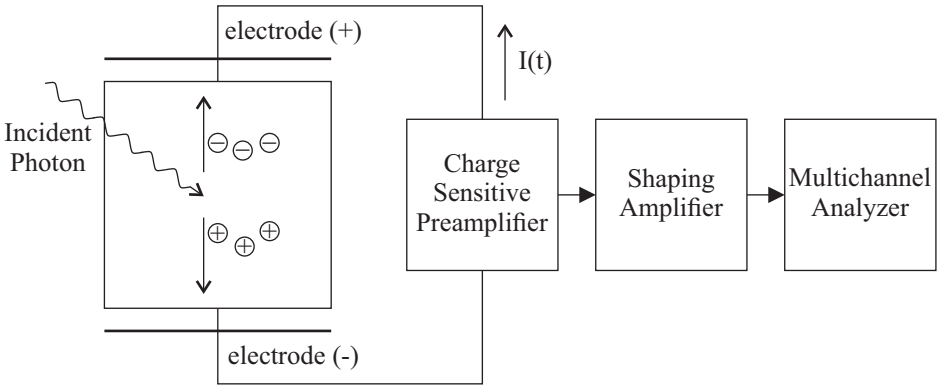

Figure 2.10: Schematic of an x-ray energy dispersive photon counting detector and electronics.

keV, 20.8 keV, 26.4 keV and 59.5 keV. CdTe detectors are known to have problems with fluorescence escape and hole tailing. The manufacturer (Amptek Inc.) quotes mean free paths of 13.2 cm for electrons and 0.8 cm for holes when the CdTe detector is operated at $\Delta V = 400$ V. Hole tailing can be seen for the high intensity 59.5 keV peak as well as fluorescence escape peaks. A response function model was previously created by LeClair et al. [31] to correct for these issues.

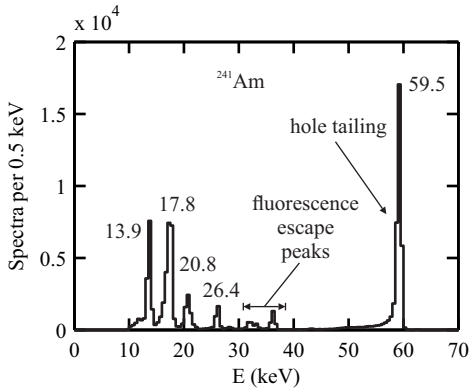

Figure 2.11: Pulse height ^{241}Am calibration spectrum measured with a CdTe detector.

Chapter 3

Methods

The validation of the WAXS fat subtraction protocol consists of estimating the $d\mu_s/d\Omega$ of the fibrous tissue within a sample ROI composed of both fat and fibrous tissue. This chapter describes the following: samples, the WAXS models, the WAXS system for conducting the WAXS measurements, the fat estimation technique which involves the use of a digital imaging system, a section devoted to explaining the data analysis. The tissue analysis was done for $\theta = 6^\circ$ and with 50 kV beams. The final section describes modifications to the WAXS system for acquisition of signals with higher kV beams and at other θ angles.

3.1 Samples

Chicken and beef tissue were acquired from a local butcher shop. Tissue was visually separated into two types: fat and fibrous tissue. These samples were labeled

as pure samples. The cylindrically shaped tissue samples of 5 mm diameter were fixed in formalin for 4 months. Following fixation, 4 mm thick homogeneous and composite samples were prepared. The composites were layered. During measurements samples were placed into a polyethylene holder as shown in Figure 3.1. The holder is shown in light gray and the tissue sample in dark gray. The region of interest (ROI) highlighted in Figure 3.1 by a black dashed line is the region from which the WAXS signals will be measured.

There is some interest in the effects the fixation process has on the measured scatter signals. Potential differences may exist based on how formalin reacts with tissue molecules and alters its structure. A brief discussion of formalin's interaction with tissue may be found in Appendix A.

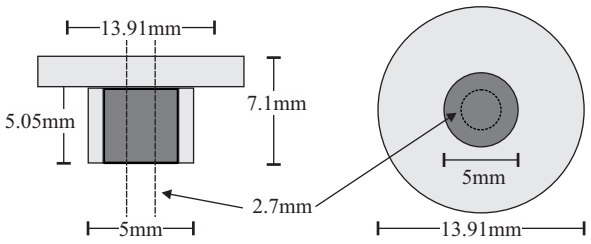

Figure 3.1: Schematic of polyethylene holder and sample.

3.2 WAXS Component

3.2.1 Models

A semianalytic model [44, 26, 29, 27, 30, 28] can be used to estimate the number of scattered photons at specific angles from tissue samples. Figure 3.2 depicts the interrogation of a portion of a 5 mm diameter thickness d biopsy with a 2.7 mm diameter 50 kV $N_0(E)$ incident beam. The sample is placed in the previously mentioned polyethylene holder and the ROI consists of a cylindrical volume defined by the intersection of the beam and sample. A CdTe energy dispersive photon counting

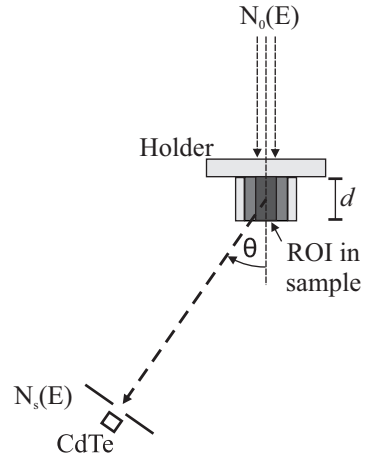

Figure 3.2: Geometry for scatter model (not to scale).

detector positioned at angle θ with respect to center of the biopsy subtends a solid angle Ω_{det} at the sample.

Suppose the tissue sample consists of both fat and fibrous tissue. Let the mean fractional volumes of fat and fibrous tissue within the ROI be $\overline{\nu}_{\text{fat}}$ and $\overline{\nu}_{\text{fib}}$, respec-

tively. The scatter coefficient of this mixture of tissue can be approximated by [44]

$$\frac{d\overline{\mu}_{\mathrm{s}}(x)}{d\Omega} = \frac{N_{\mathrm{s}}(E,\theta)}{N_0(E)\Omega_{\mathrm{det}}} \times \frac{\overline{\mu}(E)(1-\frac{1}{\cos\theta})\mathrm{e}^{\overline{\mu}(E)\frac{d}{\cos\theta}}}{[1-\mathrm{e}^{-\overline{\mu}(E)d(1-\frac{1}{\cos\theta})}]}, \tag{3.1}$$

where $N_{\mathrm{s}}(E,\theta)$ is the scatter spectrum captured with the detector, and $\overline{\mu} = \overline{\nu}_{\mathrm{fat}}\mu_{\mathrm{fat}} + \overline{\nu}_{\mathrm{fib}}\mu_{\mathrm{fib}}$. The model assumed the Compton wavelength shift to be negligible (ex. for a 30 keV incident photon scattered at $\theta = 12^{\circ}$ the energy of the Compton scattered photon is 29.96 keV.) $N_{\mathrm{s}}(E,\theta)$ to consist of incident photons which have scattered along the central axis of the sample all with angle θ. From this measurement, the $d\mu_{\mathrm{s}}/d\Omega$ of fib can be approximated by

$$\left(\frac{d\mu_{\mathrm{sc}}}{d\Omega}\right)_{\mathrm{fib}} = \frac{\left[\frac{d\overline{\mu}_{\mathrm{s}}}{d\Omega} - \overline{\nu}_{\mathrm{fat}}\left(\frac{d\mu_{\mathrm{s}}}{d\Omega}\right)_{\mathrm{fat}}\right]}{\overline{\nu}_{\mathrm{fib}}}, \tag{3.2}$$

where the subscript "c" denotes that the $d\mu_{\mathrm{s}}/d\Omega$ was obtained via subtraction (correction) of fat and $(d\mu_{\mathrm{s}}/d\Omega)_{\mathrm{fat}}$ is the scatter coefficient for a pure sample of fat. The $\overline{\nu}_{\mathrm{fat}}$ within the ROI of composite samples was estimated via a technique to be described in Section 3.3.1. An agreement between $(d\mu_{\mathrm{sc}}/d\Omega)_{\mathrm{fib}}$ and $(d\mu_{\mathrm{s}}/d\Omega)_{\mathrm{fib}}$ obtained using a pure sample of fib would validate the fat subtraction protocol. As a note, in Ref. [44] the symbol used for $d\mu_{\mathrm{s}}/d\Omega$ was μ_{s}. The new notation is more representative of a differential linear scattering coefficient.

Values of μ were needed for the application of the WAXS fat subtraction protocol (i.e. Eqs. 3.1, 3.2, and later 3.11). Two sets of μ values were used: (1) μ values

of breast fat and fib measured by Johns and Yaffe [19] were used to approximate those of animal tissue and (2) values were experimentally measured via the technique described in Section 3.2.3.2. Results obtained with the former were labeled via use of μ-breast whereas the latter via μ-expt.

3.2.2 Simulations

A C++ program was created which would allow the verification of various aspects of the WAXS model. A voxelated cube was generated which could be filled with any material. Voxels could be customized as square or rectangular and the angle of scattering adjusted. The detector could be placed at any radial distance, azimuthal and/or polar angle from the center of the cube. A non-diverging pencil beam of any radius could be set incident on the sample. The number of scattered photons from the center of each voxel, within the incident beam radius, would then be calculated and attenuated according to the path traveled to the detector.

Consider two points in 3-dimensional space; one at the location of the detector (x_D, y_D, z_D) and the other at the scatter source voxel (x_S, y_S, z_S). As seen in Fig. 3.3, showing only the x and z axes, the line passes through multiple planes on its path through the cube to the detector. First, the exit point from the cube was calculated

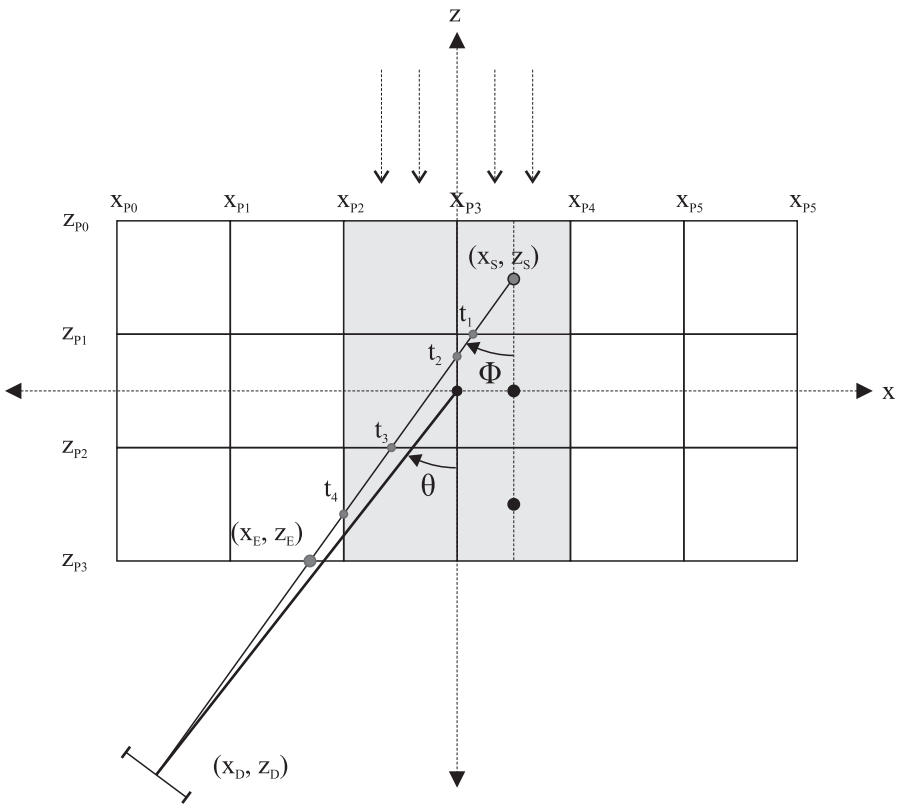

Figure 3.3: Passage of a scattered photon beamlet towards detector from the center of a voxel (not to scale). θ is the angle from the center of the biopsy and ϕ is the angle from the specific voxel.

by solving

$$\nu_z = \frac{z_P - z_S}{z_D - z_P} \tag{3.3}$$

$$\nu_x = \frac{x_P - x_S}{x_D - x_P} \tag{3.4}$$

$$\nu_y = \frac{y_P - y_S}{y_D - y_P} \tag{3.5}$$

where x_P, y_P and z_P are the possible exit planes for the beam. By finding the smallest value which satisfies $\nu \in [0,1]$ the exit point (x_E, y_E, z_E) out of the cube was calculated via

$$z_E = z_S + \nu \cdot (z_D - z_P) \tag{3.6}$$

$$x_E = x_S + \nu \cdot (x_D - x_P) \tag{3.7}$$

$$y_E = y_S + \nu \cdot (y_D - y_P). \tag{3.8}$$

Similarly, by solving for all the ν-values which satisfy $\nu \in [0,1]$ for all the x, y and z planes the distance traveled in each voxel may be found. Furthermore, by knowing which planes the beamlet passes through it is also possible to keep track of the material by which is must be attenuated.

Consider the 5 mm diameter 4 mm thick sample shown in Fig. 3.4(a) which was filled with fib and fat tissue voxels. The samples were divided into $0.1 \times 0.1 \times 0.1$ mm^3 voxels of which 22400 (560×40) occupied the central ROI (regions 1 and 2). The ROI voxels were filled three different ways: (i) region 1 consisted of tissue columns with $\nu_{fib} = 0.6/\nu_{fat} = 0.4$, region 2 with 0.4fib/0.6fat, (ii) region 1: 0.4fib/0.6fat, region 2: 0.6fib/0.4fat, and (iii) tissue columns in the ROI were filled such that their ν_{fat} distribution was a Gaussian ($\overline{\nu}_{fat} = 0.5$, $\sigma = 0.08$).

The volume of the ROI consisted of 50 % fib and 50 % fat for all cases. The voxels within each column were filled randomly. For configurations i and ii the column's ν_{fat} distributions within the ROI were dual peaked whereas Gaussian shaped for iii. As

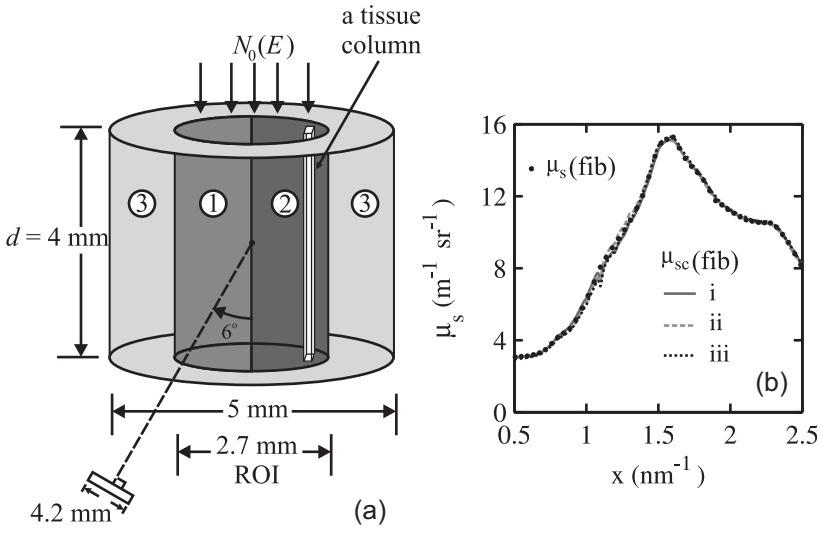

Figure 3.4: Tissue orientation simulation analysis; (a) schematic of three sample configurations: (i) region 1 consisted of tissue columns with $\nu_{\text{fib}} = 0.6/\nu_{\text{fat}} = 0.4$, region 2 with 0.4fib/0.6fat, (ii) region 1: 0.4fib/0.6fat, region 2: 0.6fib/0.4fat, and (iii) tissue columns in the ROI were filled such that their ν_{fat} distribution was a Gaussian ($\overline{\nu}_{\text{fat}} = 0.5$, $\sigma = 0.08$). (b) $d\mu_{\text{sc}}/d\Omega(\text{fib})$ signals via applications of the fat subtraction model.

shown later in Chapter 4.1.1, they were Gaussian distributions for the tissue samples. The outer regions labeled as 3 were filled with fib yet filling them with fat gave similar results. This indicated that the outer region composition need not be known and for the application of the WAXS models, the composition of the ROI could be used for region 3.

The scattering was assumed to occur at the center of each voxel. Only single scatter was considered and statistical noise was not included in the simulations. The coherent form factors F used in the calculations were those measured by Poletti *et al.* [38] The incoherent scattering functions S were calculated using S of atoms from Hubbell *et al.* [16] and the sum rule. The compositions used were those from Poletti

et al. [38] and $\mu = \mu$-breast. [19]

The $d\mu_{sc}/d\Omega$(fib) curves obtained via the subtraction model for the three sample configurations are shown in Fig. 3.4(b). The $d\mu_s/d\Omega$ of fib which was sought is also shown. Although there are small differences between the curves, the subtraction works regardless of which type of ν_{fat} distribution existed. The findings suggest that only $\overline{\nu}_{fat}$ is required for the application of the models and knowing the distributions of ν_{fat} within the ROI of the sample is not necessary.

3.2.3 Diffractometer System

3.2.3.1 Scatter Measurements

The WAXS system is housed in an x-ray cabinet (Model 43855C, Faxitron X-Ray Corporation, Chicago IL). It consists of a stationary anode tungsten tube, a MAGNA 1cc parallel plate chamber and SuperMAX electrometer (Standard Imaging Inc., Middleton WI), pinhole apertures, translation and rotation stages (Unislide Model, Velmex Inc., Bloomfield NY), and a cadmium telluride (CdTe) 25 mm^2 by 1 mm thick crystal (XR-100T-CdTe, Amptek Inc., Bedford MA).

Figure 3.5(a) shows a schematic of the scatter geometry. A 50 kV beam 2.7 mm in diameter at the surface of the sample and of 3 min duration yielded an entrance exposure of 1.2×10^{-1} C/kg. An ion chamber provided a means to correct for tube output fluctuations. Scatter signals from the cylindrical shaped region of interest (ROI) were measured at 6° with the CdTe crystal which was collimated by a D = 4.2

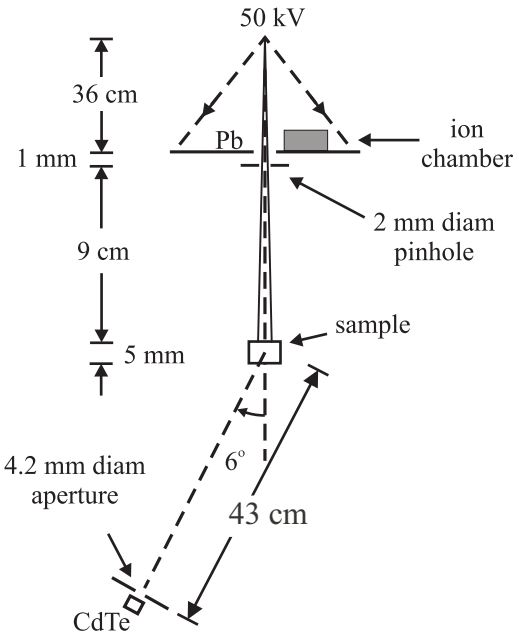

Figure 3.5: Scatter geometry for $\theta = 6°$ measurements.

mm diameter Pb aperture. The detector positioned at r = 43 cm from the sample resulted in a solid angle of detection of $\Omega_{\rm det} = \pi D^2/4r^2 = 7.75 \times 10^{-5}$ sr.

Corrections for air scatter were applied to all spectra by the method described in Ref. [44]. The $N_0(E)$ spectrum was estimated using the $N_{\rm s}$ spectrum of a sample of polycarbonate. Namely Eq. 3.1 with $\overline{\mu}$ replaced by μ for a pure sample was rearranged to solve for $N_0(E)$. The scatter $d\mu_{\rm s}/d\Omega$ data measured by Kosanetzky *et al.* [23] was used for this purpose. The animal WAXS tissue results that will be presented were published in the journal *Medical Physics*. [45] In that journal article, as in this work, only the final $d\mu_{\rm s}/d\Omega$ data were shown since in Ref. [44] more details were given about the raw WAXS spectra. The acquisition of the WAXS spectra was primarily done by a collaborator. The animal tissue preparation and subsequent application of the fat

estimation technique to be described in Section 3.3 was the major focus of this work.

3.2.3.2 Transmission Measurements

Besides using μ-breast values for those of animal tissue, values were estimated experimentally with the WAXS system in the $\theta = 0^\circ$ configuration. The methodology for acquiring μ via energy dispersive measurements was presented in detail [25]. A smaller 25 μm diameter aperture was used. A two basis function [19] method with aluminum and polycarbonate as bases was used to fit μ versus energy curves for fat and fibrous tissue. To obtain the curves, a 50 kV spectrum was used and the $N_0(E)$ was estimated using a transmission measurement through a 4 mm thick PMMA sample. For an energy range 8 to 25 keV, singular value decomposition was used to solve the overdetermined system. My contribution to the μ component analysis was assistance with the data acquisition.

The results of μ measured (μ-expt) for chicken fat and fibrous were compared to those of breast tissue (μ-breast) [19] via the percent differences which are shown in Fig. 3.6. The results suggest that μ values of chicken tissue are similar to those of breast tissue. The differences (e.g. for chicken fat -5.8% smaller at 19 keV) could be caused by the fact that the samples were fixed in formalin whereas those used by Johns and Yaffe [19] were unfixed tissue specimens. It is believed that the duration between sample extraction from formalin solution to actual transmission measurement need to be monitored. Values of μ for beef were measured but deemed unacceptable because

of this duration. The WAXS fat subtraction protocol with beef tissue was only done with μ-breast values. Although optimization of μ measurements will be needed, the results obtained were interesting and encouraging.

3.3 Fat Estimation Component

Different methods have been used to assess the fibroglandular/fat content (breast density) in vivo since the knowledge provides a way to estimate the risks of developing cancer. [50, 51, 32, 7, 47, 53] As Yaffe [52] summarizes, different qualitative and quantitative methods have been applied to evaluate breast density. Examples of visual classification methods are the Wolfe density categories [50] and the Breast Imaging Reporting and Data System (BI-RADS). [12] More reliable computer-aided breast density measurements for quantitative analysis were developed. [15] The grey level thresholding method is a two-dimensional technique where either a radiologist or a fully automated computer-assisted segmentation software chooses the threshold level to categorize the dense versus non-dense regions. Three-dimensional x-ray breast imaging techniques may prove to be more useful since they overcome the limitations of overlapping structures. Dedicated breast CT [6, 34] and breast tomosynthesis [42] are two methods that are currently under development.

Although the task to estimate breast density in a breast biopsy is simpler, it is not trivial. Histology analysis of thin (e.g. 5 μm) sections of tissue can be used to estimate the composition of samples (e.g. Ref. [21]). There is, however, no guarantee the

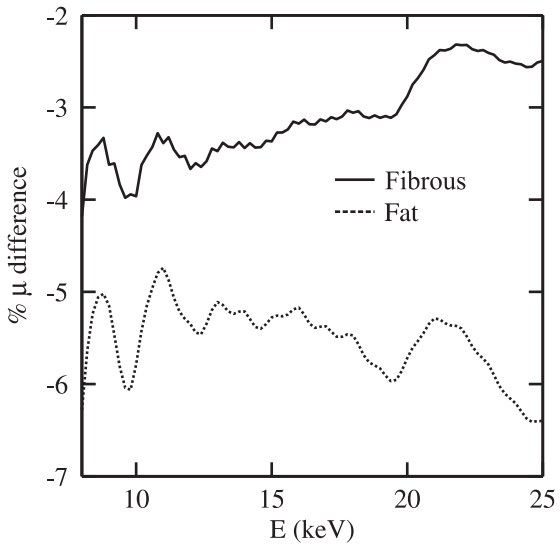

Figure 3.6: Comparisons of μ for chicken versus breast[33] [19] tissue.

composition of the chosen slice(s) is the same throughout the sample. Geraki *et al.* [13] used XRF and energy dispersive x-ray diffraction (EDXRD) for the quantification of elemental concentrations in breast tissue. They found elevated concentrations of iron, copper, zinc and potassium in malignant specimens.

Because the attenuation coefficients (μ) of fat are significantly different from those of cancer and fibroglandular tissue, [19] an x-ray imaging method was used to estimate $\overline{\nu}_{\text{fat}}$ in the volume of tissue (i.e. ROI) that was interrogated during the WAXS measurement. An ROI with animal fat and fib tissue was used in this work.

3.3.1 Imaging System

The fat estimation technique entails the generation of digital x-ray images of the tissue samples with the MX-20 digital specimen radiography system described pre-

viously in Section 2.3.1. The focal spot size was 25 μm and there are 1024 by 1024 square 24.8 μm detector pixels. The samples were imaged at a magnification 2 using 26 kV, 0.3 mA, and 3.8 sec exposure times. The entrance exposure per image was 9.2×10^{-4} C/kg.

The MX-20 was calibrated with polyethylene (polyet) and polymethyl methacrylate (PMMA) samples each 5 mm in diameter and thicknesses ranging from 1 to 5 mm. The energy incident signal (EIS) upon a given pixel of area A_{pixel} was calculated using

$$\text{EIS} = \sum_{\text{j}} E_{\text{j}} \Phi_0(E_{\text{j}}) A_{\text{pixel}} e^{-(\mu_{\text{polyet}}(E_{\text{j}}) d_{\text{polyet}} + \mu_{\text{PMMA}}(E_{\text{j}}) d_{\text{PMMA}})}, \tag{3.9}$$

where the incident photon fluence $\Phi_0(E)$ at the sample surface (shown previously in Fig. 2.3) was estimated using a CdTe detector collimated with a 25 μm diameter tungsten aperture. The μ values were calculated using cross section data for elements of Plechaty et al. [37] and the sum rule. [27] The CCD detector pixel values are denoted by ADU to represent Analogue to Digital Units i.e. a digital number which corresponds to the amplitude of the signal generated at the pixel. Figure 3.7(a) shows the calibration curve fitted with a line of best fit given by

$$\text{ADU}_{\text{fit}}(\text{EIS}) = \text{m} \times \text{EIS} + \text{b}, \tag{3.10}$$

where $\text{m} = (7.72 \pm 0.13) \times 10^{-3}$ ADU/keV and $\text{b} = (-31.3 \pm 34.1)$ ADU.

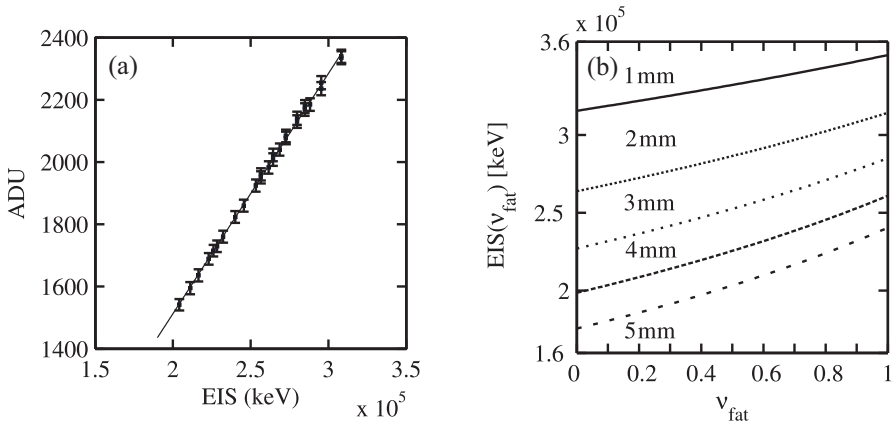

Figure 3.7: Calibration curves (a) ADU versus EIS using PMMA and polyet plastics and (b) EIS versus ν_{fat} for various thicknesses.

3.3.2 Fat Estimation Technique

The $\overline{\nu}_{\text{fat}}$ within the 2.7 mm diameter 4 mm thick ROI was determined as follows. Consider the columns of tissue defined by the intersections of beamlets and pixels. Within the ROI there were 9533 columns. Each tissue column of thickness d was assumed to be composed of a mixture of fibrous and fat tissue. Let ν_{fat} denote the fractional volume of fat for a particular column. Calculations of

$$\text{EIS}(v_{\text{fat}}) = \sum_{\text{j}=1} E_{\text{j}} \Phi_0(E_{\text{j}}) A_{\text{pixel}} e^{-(\mu_{\text{fib}}(E_{\text{j}})(1-v_{\text{fat}})+\mu_{\text{fat}}(E_{\text{j}})v_{\text{fat}})d}, \tag{3.11}$$

as a function of ν_{fat} ranging from 0 to 1 were calculated using the attenuation coefficients μ of breast tissue. [19] Figure 3.7(b) shows plots of $\text{EIS}(\nu_{\text{fat}})$ versus ν_{fat} for samples of thickness d = 1, 2, 3, 4 and 5 mm. The line corresponding to d = 4 mm was used in this work to estimate ν_{fat} for each column of tissue. Note that

for whatever thickness of biopsy one can generate the required EIS(ν_{fat}) versus ν_{fat} curve. The calculated EIS(ν_{fat}) (Eq. 3.11) that matched the EIS obtained via the ADU-EIS calibration (rearrangement of Eq. 3.10 with ADU_{fit} replaced with the ADU pixel value) yielded ν_{fat} for the column. The mean value $\overline{\nu}_{\text{fat}}$ was calculated for the ROI and its uncertainty was estimated as follows. EIS lower and upper bounds were calculated, namely,

$$\text{EIS}^{\text{lower}} = \text{EIS} - \sigma_{\text{c}}, \tag{3.12}$$

$$\text{EIS}^{\text{upper}} = \text{EIS} + \sigma_{\text{c}}, \tag{3.13}$$

per pixel, where

$$\sigma_{\text{c}}^2 = \left(\frac{\partial \text{EIS}}{\partial \text{m}}\right)^2 \sigma_{\text{m}}^2 + \left(\frac{\partial \text{EIS}}{\partial \text{b}}\right)^2 \sigma_{\text{b}}^2 + \left(\frac{\partial \text{EIS}}{\partial \text{ADU}}\right)^2 \sigma_{\text{ADU}}^2 - 2\text{mb Cov}(\text{m}, \text{b}). \tag{3.14}$$

The error in ADU units ($\sigma_{\text{ADU}} = 19.9$) was taken to be the mean value of the standard deviations of ROI pixels values for all plastic samples. From the calibration curve [Fig. 3.7(b)], corresponding ν_{fat} bounds were extracted per pixel. The means of the bounds were taken and their differences from $\overline{\nu}_{\text{fat}}$ provided an uncertainty range.

Figure 3.8(a) shows an image of a PMMA sample. The dashed white line in the image was added to highlight the ROI that corresponds to a 2.7 mm diameter central region. Since the thickness and purity of the plastic sample is accurately known it may be used as a reference for those qualities. Fig. 3.8 (b) shows the corresponding histogram of the ADU values within the ROI. The mean and standard deviation is

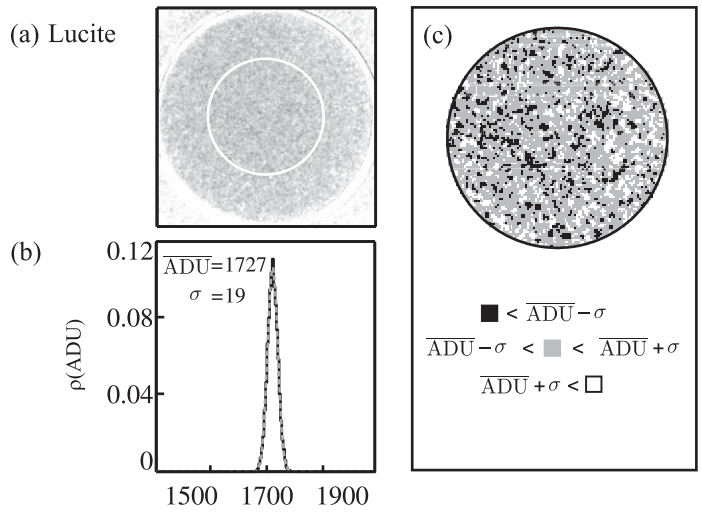

Figure 3.8: Analysis of PMMA through (a) digital x-ray image, (b) ADU histogram, and (c) ADU map.

given and was used to plot the Gaussian distribution (dashed line). The Gaussian approximates the distribution which implies purity and a uniform surface. Fig. 3.8(c) shows the ADU map. Pixels are displayed as gray unless they have an ADU beyond 1σ of the mean, in which case as black ($<$) or white ($>$). The maps are meant to highlight any possible features within the ROI that would appear as clustered regions. The map for PMMA displays a mottle pattern. The features seen for the PMMA sample may be used as a contrast to those of tissue.

3.4 Data Analysis

Quantitative methods to analyze the resultant $d\mu_s/d\Omega$ curves were accomplished using a student t-test. For assessing the applicability of Eq. 3.1 for composite samples

consisting of fat and fib mixtures (mix), the following expression was evaluated

$$\left(\frac{d\overline{\mu}_{\mathrm{s}}(x)}{d\Omega}\right)^{\Sigma} = \overline{\nu}_{\mathrm{fat}}\left(\frac{d\mu_{\mathrm{s}}(x)}{d\Omega}\right)_{\mathrm{fat}} + \overline{\nu}_{\mathrm{fib}}\left(\frac{d\mu_{\mathrm{s}}(x)}{d\Omega}\right)_{\mathrm{fib}}. \tag{3.15}$$

Agreements between $d\overline{\mu}_{\mathrm{s}}/d\Omega$ and $(d\overline{\mu}_{\mathrm{s}}/d\Omega)^{\Sigma}$ could suggest that both are good representations of the scattering coefficients for composite samples. The $d\mu_{\mathrm{s}}/d\Omega$ of fib obtained via the fat subtraction protocol, namely, $d\mu_{\mathrm{sc}}/d\Omega$ was compared to $d\mu_{\mathrm{s}}/d\Omega$ obtained with a pure sample. The following differences were computed as a function of x

$$\Delta_{\mathrm{mix}}(x) = \left(\frac{d\overline{\mu}_{\mathrm{s}}(x)}{d\Omega}\right) - \left(\frac{d\overline{\mu}_{\mathrm{s}}(x)}{d\Omega}\right)^{\Sigma} \tag{3.16}$$

and

$$\Delta_{\mathrm{fib}}(x) = \left(\frac{d\mu_{\mathrm{sc}}(x)}{d\Omega}\right)_{\mathrm{fib}} - \left(\frac{d\mu_{\mathrm{s}}(x)}{d\Omega}\right)_{\mathrm{fib}}. \tag{3.17}$$

The uncertainties in the Δs were approximated respectively by

$$\sigma[\Delta_{\mathrm{mix}}(x)] = \sqrt{\sigma^2[\left(\frac{d\overline{\mu}_{\mathrm{s}}(x)}{d\Omega}\right)] + \sigma^2[\left(\frac{d\overline{\mu}_{\mathrm{s}}(x)}{d\Omega}\right)^{\Sigma}]} \tag{3.18}$$

and

$$\sigma[\Delta_{\mathrm{fib}}(x)] = \sqrt{\sigma^2[\left(\frac{d\mu_{\mathrm{sc}}(x)}{d\Omega}\right)_{\mathrm{fib}}] + \sigma^2[\left(\frac{d\mu_{\mathrm{s}}(x)}{d\Omega}\right)_{\mathrm{fib}}]}. \tag{3.19}$$

A two-sided one-sample t-test was used to determine whether there was a significant difference between the mean of the population (e.g. $\Delta_{\mathrm{mix}}(x)$ data points) and the expected values which were chosen as 0 since if they matched the mean differ-

ence between curves would be nil. A null hypothesis (expected mean) may then be rejected with a desired confidence level. The calculated Δ values should have had no dependence on the momentum transfer argument, therefore, were assumed to have a normal (Gaussian) distribution. The t-test is usually applied to such distributions, however, it is not necessary for it to be applicable. The t-values were calculated via

$$\mathrm{t(mix)} = \frac{<\Delta_{\mathrm{mix}}> - 0}{\sqrt{\sigma^2[\Delta_{\mathrm{mix}}(\mathrm{x})]/\mathrm{n}}} \tag{3.20}$$

$$\mathrm{t(fib)} = \frac{<\Delta_{\mathrm{fib}}> - 0}{\sqrt{\sigma^2[\Delta_{\mathrm{fib}}(\mathrm{x})]/\mathrm{n}}} \tag{3.21}$$

where the $<\Delta>$s are expectation values for the populations, n is the population size and σ is the standard deviation. Table 3.1 shows the two-tailed t-table which was employed to find the critical value ($\mathrm{t_c}$) for the given degrees of freedom, $\mathrm{df} = \mathrm{n} - 1$, and the desired probability level p. If the calculated t-value was greater than $\mathrm{t_c}$ the null hypothesis for $\mathrm{p} < 0.05$ could be rejected with a 95% confidence level. $\mathrm{p} < 0.05$ is a standard scientifically accepted level of confidence.

df	p<0.10	p<0.05	p<0.01
1	6.314	12.706	63.657
2	2.920	4.303	9.925
...			
29	1.699	2.045	2.756
30	1.697	2.042	2.750
40	1.684	2.021	2.704

Table 3.1: Student's two tailed t-test distribution table [48] where df is the degrees of freedom.

The root mean square deviation (Δ_{RMS}) given by

$$\Delta_{\mathrm{RMS}}^{\mathrm{mix}} = \sqrt{\frac{1}{\mathrm{n}}(\Delta_{\mathrm{mix}}^2(x_1) + \Delta_{\mathrm{mix}}^2(x_2) + ... + \Delta_{\mathrm{mix}}^2(x_n)} \tag{3.22}$$

and

$$\Delta_{\mathrm{RMS}}^{\mathrm{fib}} = \sqrt{\frac{1}{\mathrm{n}}(\Delta_{\mathrm{fib}}^2(x_1) + \Delta_{\mathrm{fib}}^2(x_2) + ... + \Delta_{\mathrm{fib}}^2(x_n)} \tag{3.23}$$

were also calculated. The Δ_{RMS} is calculated for a varying quantity and is a measure of its magnitude.

3.5 Diffractometer System Modifications

The WAXS measurements with animal tissue were obtained using $\theta = 6°$ and a 50 kV beam resulting in an momentum transfer range of 0.3 nm^{-1} to 2.11 nm^{-1}. Figure 3.9(a) shows the $d\mu_{\mathrm{s}}/d\Omega$ of water, PMMA and polycarbonate calculated using S and F values from literature, $\theta = 6°$ and $E = 0$ to 50 keV. Modifying the WAXS system to allow measurements at 80 kV would result in a larger x-space. Figure 3.9(b) shows $d\mu_{\mathrm{s}}/d\Omega$ obtained at $\theta = 6°$ using $E = 0$ to 80 keV. An overlap may be obtained in the x range by using various angles. Low angles such as $\theta = 2°$ [Fig. 3.9(c)] and high angles such as $\theta = 12°$ [(Fig. 3.9(d)] make x = 0.11 to 6.74 nm^{-1} accessible. The use of larger angles with an 80 kV beam results in scatter signals with larger x values where diffraction plays a smaller role. In this work the focus was on extending the x

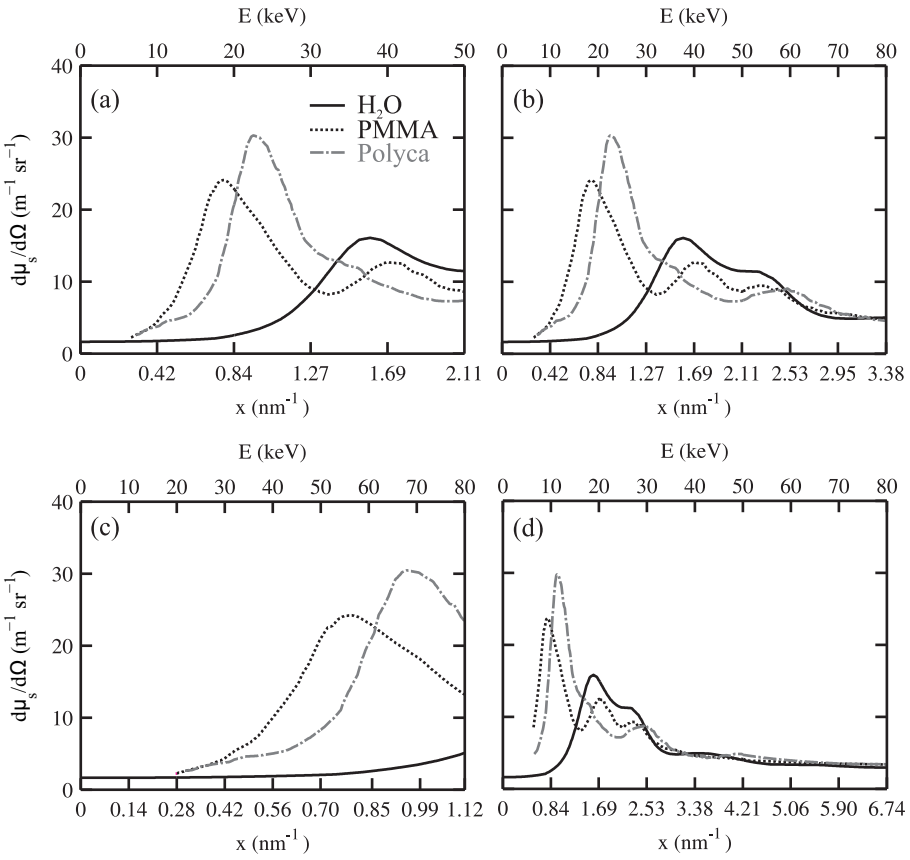

Figure 3.9: $d\mu_s/d\Omega$ of PMMA, water and polycarbonate calculated using F and S from literature: (a) $\theta = 6°$, $E = 0$ to 50 keV, and $E = 0$ to 80 keV for (b) $\theta = 6°$, (c) $\theta = 2°$, and (d) $\theta = 12°$.

range with 80 kV beams and the acquisition of scatter information at various angles; $\theta = 2°$, $6°$, $8°$, $12°$ and $16°$. A description of the modifications to the system follow.

Figure 3.10 shows a schematic of the new geometry in the x ray cabinet. The beam was 3.3 mm in diameter at the surface of the sample. A minimum of 3 cm of lead was added to all the shelves in the system to prevent any transmission as a result of the 80 kV potential. A 70 keV photon has a 2 % chance of penetrating 1 cm of lead. Two setups were implemented: setup 1 employed the use of lead sample

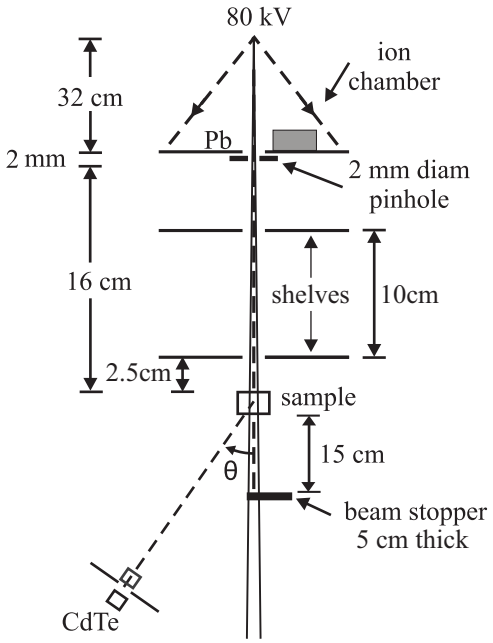

Figure 3.10: Optimized WAXS scatter geometry.

holder and a bass collimator assembly at the detector while setup 2 consisted of a polyethylene holder with a 4.2 mm lead aperture on top and a 3 mm diameter Pb aperture on the detector cap. The sample holders and collimators at the detector for both setups are shown in Figure 3.5. The 3 mm diameter lead aperture 0.7 mm thick at the top of a 3.6 cm brass cylinder with 1 mm thick walls, a second lead aperture 4.2 mm in diameter 0.5 mm thick followed by the detector cap which mounts onto the CdTe housing unit narrowed the field of view of the detector.

Contamination due to scatter from the pinhole was addressed by B.Sc student Dex Kouna who began modifications on the system as described in his fourth year thesis [24]. The procedure was to elevate the pinhole and add a lead aperture at the polyethylene sample holder (set-up 1) to accommodate measurements at smaller

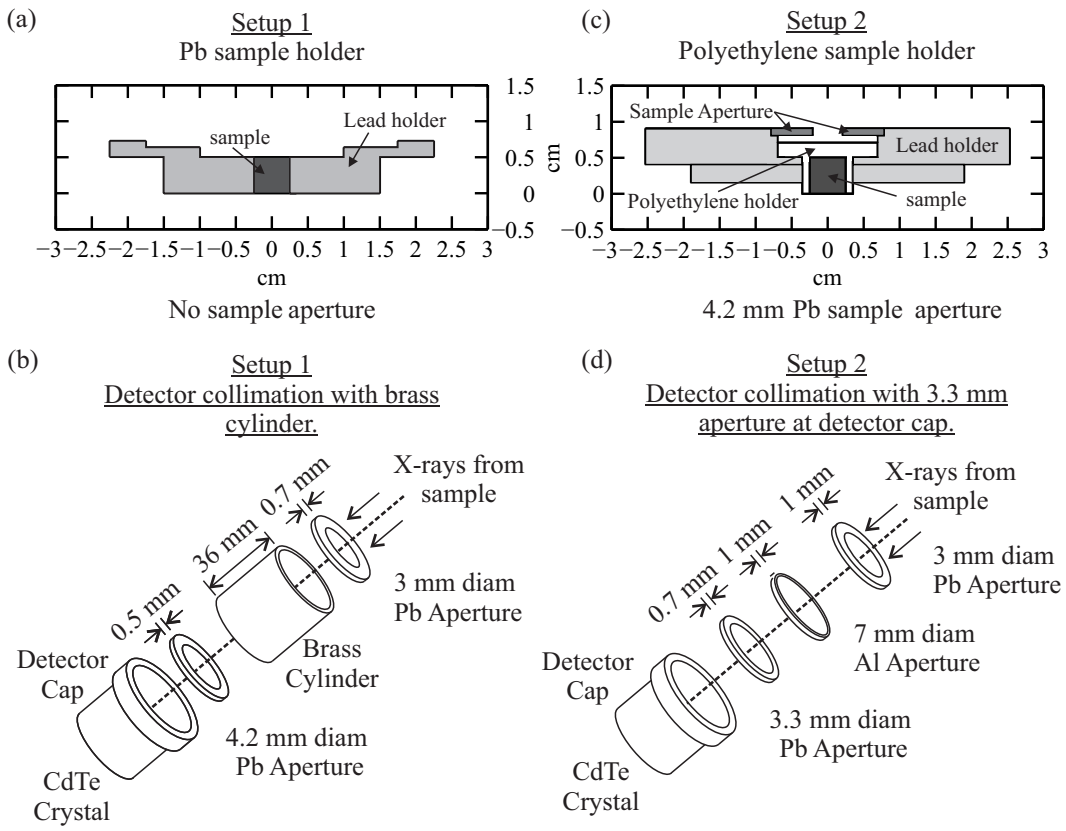

Figure 3.11: (a,c) Sample holders and (b,d) detector collimators. (a) and (b) for setup 1 and (c) and (d) for setup 2.

angles. The increased distance between the pinhole and sample resulted in a less direct path for pinhole scatter to reach the detector. Adding the sample aperture blocked the pinhole scatter that would have a direct path to the detector through the sample. The greater thickness of lead when using the lead sample holder would prevent any unwanted scatter originating from the pinhole from being transmitted through the holder.

The geometry within the x-ray cabinet was modeled using Matlab and Fig. 3.12 shows the path at the lead holder sample (set-up 2) location of the pinhole scatter

that heads towards the detector for a (a) 2°, (b) 6° and (c) 12° system orientation. The positioning of all the apertures within the cabinet is well known; allowing for small angle measurements down to 2°. For angles greater than and including 12° there is no direct path for scatter from the pinhole to reach the detector. Therefore, higher angles are not shown since the photons would need to travel through multiple shelves lined with lead.

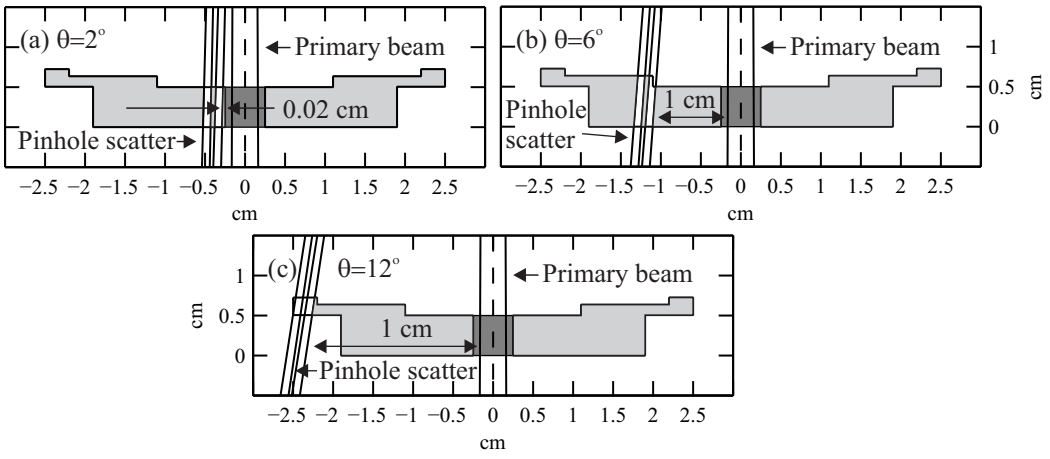

Figure 3.12: Pinhole scatter which heads directly towards the detector for (a) $\theta = 2°$, (b) $\theta = 6°$ and (c) $\theta = 12°$. For all higher angles the direct path to the detector would require transmission through shelve(s).

A beam stopper was added so as to minimize air scatter contamination from the primary beam. The beam stopper was positioned at a location which would not block the useful scatter from the sample. As illustrated in Fig. 3.10 a 5 cm thick beam stopper could be moved into position to minimize air scatter contributions from the primary beam after passing through the sample which could further be scattered towards the detector. It was important that the beam stopper did not intrude into the

path of the scattered beam, therefore, careful geometric measurements were done. The beam stopper was positioned 15 cm below the sample for $\theta < 9^\circ$ while a second identical beam stopper can be placed into the primary beam for higher angles at a distance of 5 cm below the sample (not shown in Fig.3.10.)

Figure 3.13 shows the path of scatter originating in the sample and heading towards the edges of the detector for $\theta = 2^\circ$ and $\theta = 6^\circ$. Figure 3.13(a) illustrates a wider view of the system including the sample holder as well as the beam stopper for 6°, (b) and (c) are close ups of the scatter path at the location of the beam stopper for $\theta = 2^\circ$ and $\theta = 6^\circ$, respectively. The most crucial system alignment was necessary for $\theta = 2^\circ$ measurements since the scatter path and beam stopper only have a distance of 0.06 cm between them.

An estimation of the air scatter was done using the Matlab software and the scatter model described previously. The ratio of the estimated scatter with to without the beam stopper was taken at various angles. The mean of the ratio at $\theta =$ 2°, 6°, 8°, 12° and 16° were 0.51, 0.54, 0.52, 0.48 and 0.47, respectively. Therefore, it is anticipated that in an ideal situation the background due to air scatter can be reduced by approximately 0.5.

Another feature the software provided was the ability to address the possibility of scatter from the sample being attenuated by the sample holder. Figure 3.14 shows a $\theta = 16^\circ$ scatter beam. Note that using a 5 mm sample [Fig. 3.14(a)] would result in scatter beam attenuation, therefore, for this particular orientation sample thickness

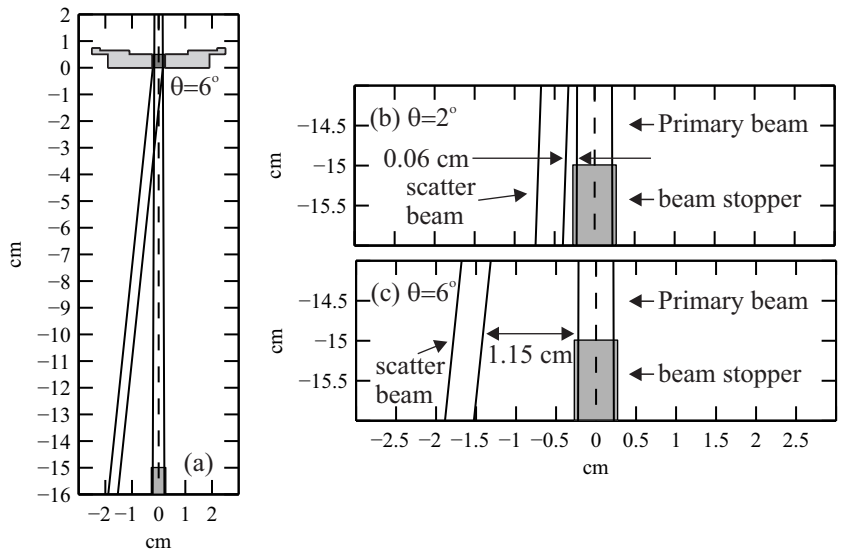

Figure 3.13: Path of scatter from a 5 mm thick sample at beam stopper position. (a) View of sample and beam stopper for $\theta = 6°$, close ups of scatter path and beam stopper for (b) $\theta = 2°$ and (c) $\theta = 6°$. For all higher angles the distance between scatter path and beam stopper is large.

of 3 mm or less must be used [Fig. 3.14(b)].

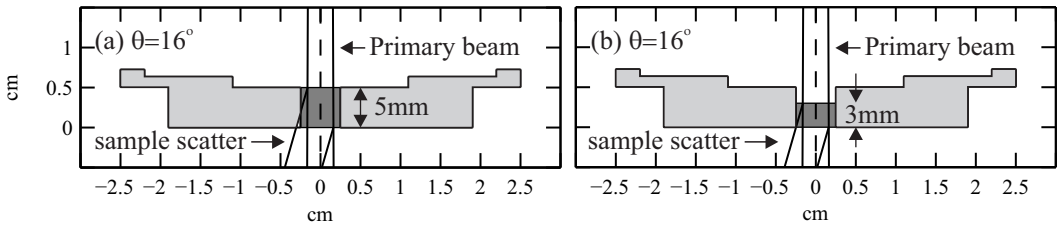

Figure 3.14: Path at sample of scatter at $\theta = 16°$ for (a) 5 mm versus (b) 3 mm sample. Close up of the sample.

The samples used for the 80 kV analysis were PMMA, polycarbonate, and water.

Chapter 4

Results

The culminated results obtained using the methods described in the previous chapter are presented. The first section presents the results obtained with the animal tissue. This section is subdivided as follows: (1) images of the tissue samples which were used to estimate $\overline{\nu}_{\text{fat}}$, (2) measured $d\mu_s/d\Omega$ signatures of fat and fibrous tissue compared to data from other groups and (3) results obtained with the fat subtraction model. The second section contains $d\mu_s/d\Omega$ results obtained using an 80 kV beam and different θs for samples of water, PMMA, and polycarbonate.

4.1 Animal Tissue

4.1.1 Images

Figure 4.1 shows digital images of chicken (i) fat, (ii) fibrous, (iii) composite as well as beef (iv) fat, (v) fibrous, and (vi) composite. The digital images show that the thickness of tissue at the outer edges varied a lot especially for the fibrous and the chicken composite samples. With better tissue preparation, the shape of the samples will look more like that of the plastic sample [Fig. 3.8(a)]. However, it is the $d\mu_s/d\Omega$ of the tissue within the ROI which was sought via WAXS measurements. The material outside the ROI, as mentioned in Section 3.2.2, was involved only in attenuating a small portion of the scattered photons from reaching the CdTe detector during the WAXS measurements. The beef fibrous image has some white streaks suspected to be caused by fat tissue.

Figures 4.1(b)(i) to (vi) show the corresponding histograms of the ADU values within the ROI. The Gaussians approximate the distributions except for the chicken fibrous sample [Fig. 4.1(b)(ii)]. This sample's ROI thickness deviated from uniformity. In a future work, a new tissue cutting apparatus will provide consistently uniform thicknesses for the samples.

Figures 4.1(c)(i) to (vi) show ADU maps. In contrast to the PMMA map [Fig. 3.8(c)] those of the tissues have mottle characteristics yet some clustering is seen. The map for beef fibrous [Fig. 4.1(c)(v)] has clusters caused by fat streaks

while the larger clusters occurring for chicken fibrous [Fig. 4.1(c)(ii)] were caused by a non-uniform thickness. Although deviations from purity and thickness uniformity occurred, the WAXS results shown below for all samples were encouraging.

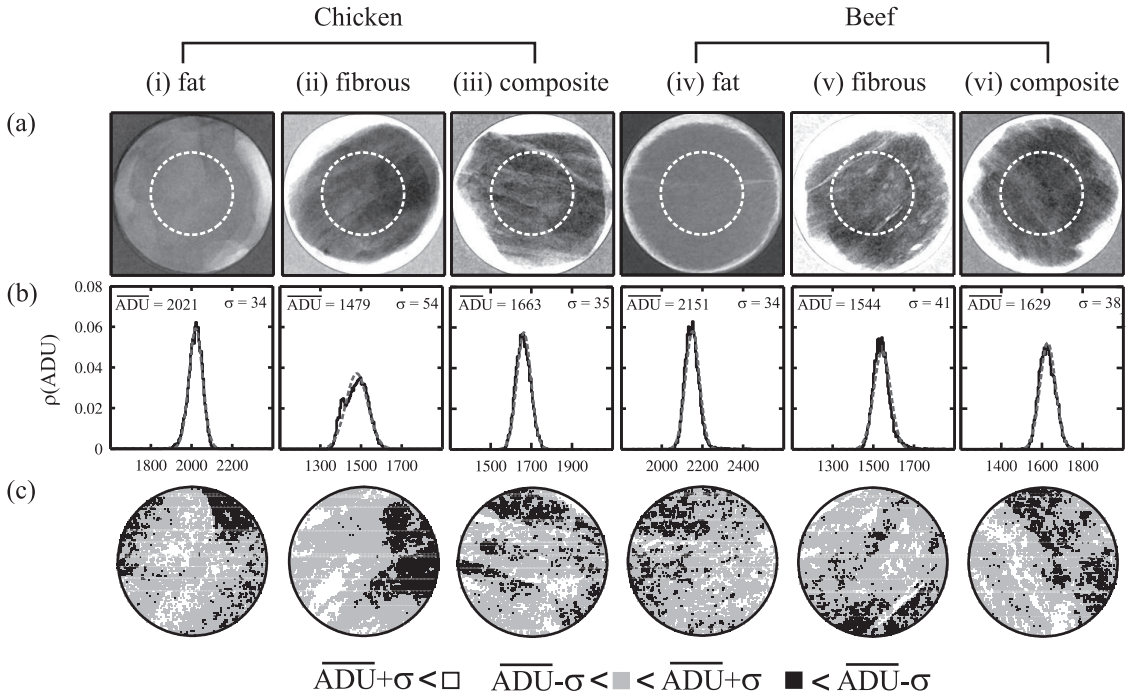

Figure 4.1: (a) Digital x-ray images, (b) ADU histograms, and (c) ADU maps of chicken and beef samples.

4.1.2 μ_s of "Pure" Samples

Figure 4.2 shows the $d\mu_s/d\Omega$ values for tissue (a) fat and (b) fibrous samples. Panels (i) and (ii) are for chicken using μ-breast and μ-expt, respectively. Panel (iii) is for beef tissue using μ-breast. Also shown are $d\mu_s/d\Omega$ for breast tissue from Kidane *et al.*, [21] $d\mu_s/d\Omega$ for breast tissue calculated using F data from Poletti *et al.*, [38] S from Hubbell *et al.* [16] with compositions from Poletti *et al.*; [38] and $d\mu_s/d\Omega$ for

animal tissue calculated using F data from Peplow and Verghese, [10] S from Hubbell *et al.* [16] with compositions from ICRU Report 46. [17] The 1.1 nm^{-1} fat peak signal is seen in the fat samples. The fibrous data are similar to each other except for the Kidane *et al.* [21] fibroglandular breast tissue.

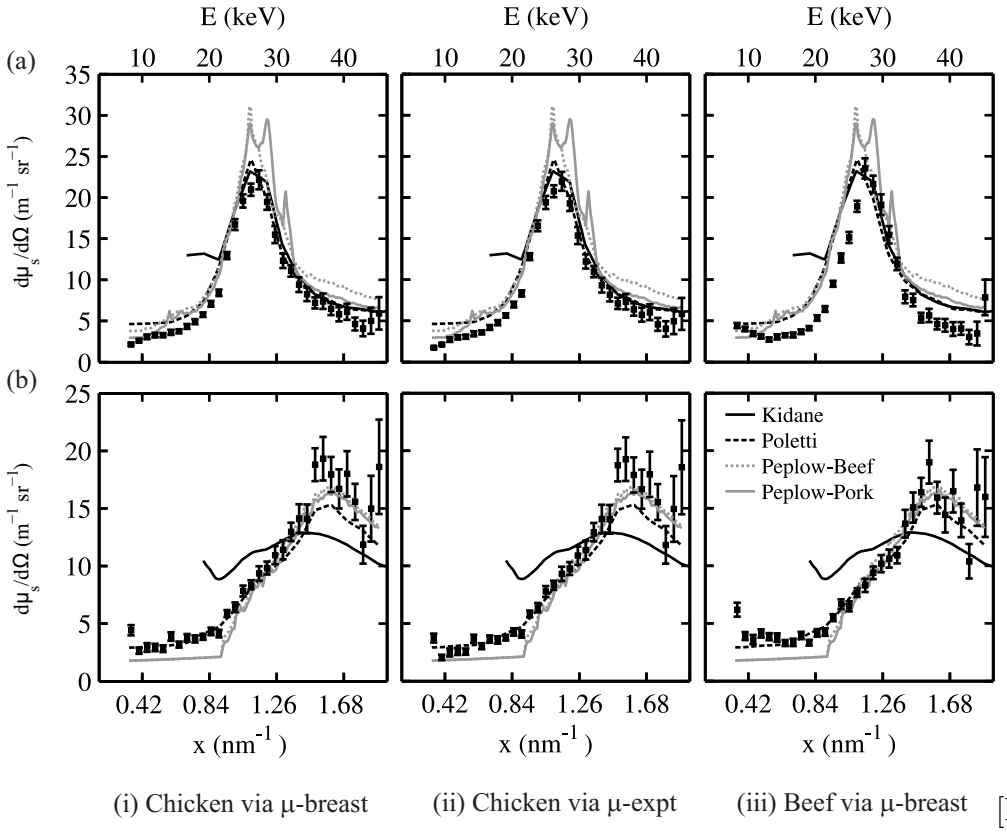

[ht]

Figure 4.2: $d\mu_s/d\Omega$ of (a) fat and (b) fibrous tissue of chicken via (i) μ-breast, (ii) μ-expt and beef (iii) via μ-breast.

4.1.3 Fat Subtraction Data

Figure 4.3 shows the ν_{fat} distributions for the chicken and beef composites. The ROIs' ν_{fat} distributions were well approximated by Gaussians (dashed lines) obtained

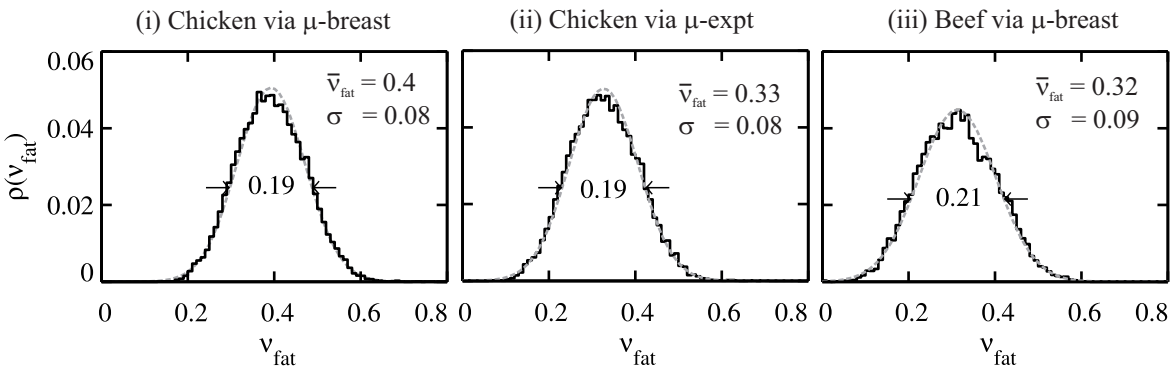

Figure 4.3: ν_{fat} distributions of chicken and beef composites. The estimation was applied to (i) chicken via μ-breast, (ii) chicken via μ-expt and (iii) beef via μ-breast.

using the $\overline{\nu}_{\text{fat}}$ and σs (see figure) of each distribution. The FWHMs are indicated via the arrows. For the chicken composite, $\overline{\nu}_{\text{fat}} = 0.4 \pm 0.05$ via use of μ-breast, 0.33 ± 0.05 using μ-expt, and 0.32 ± 0.05 for the beef composite using μ-breast.

Figure 4.4(a) shows that $d\overline{\mu}_{\text{s}}/d\Omega$ matches well with $(d\overline{\mu}_{\text{s}}/d\Omega)^{\Sigma}$ for the composite samples. The results for chicken were slightly better when μ-expt were used. These are the results for the composite samples for which the fat subtraction model were applied to.

Figure 4.4(b) shows that $(d\mu_{\text{sc}}/d\Omega)_{\text{fib}}$ obtained via the fat subtraction model matched closely the $(d\mu_{\text{s}}/d\Omega)_{\text{fib}}$ obtained with a pure fibrous sample. Again for chicken, better results were obtained using μ-expt. Although the results for beef with μ-expt were poor (not shown) the results obtained using μ-breast were satisfactory. The findings validate the use of the technique for estimating $\overline{\nu}_{\text{fat}}$ for the applications of the WAXS models.

Figure 4.5(a) and (b) show Δ_{mix} and Δ_{fib}, respectively, for chicken via (i) μ-

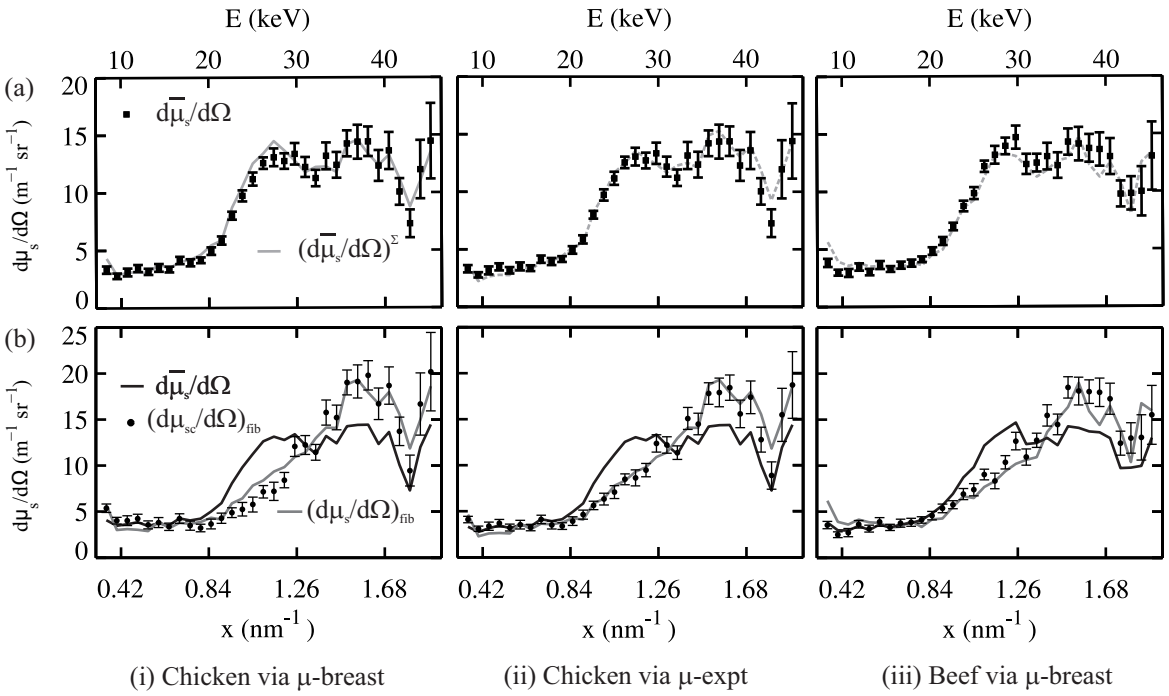

Figure 4.4: (a) $d\overline{\mu}_{\rm s}/d\Omega$ and $(d\overline{\mu}_{\rm s}/d\Omega)^{\Sigma}$ of composite samples and (b) $d\mu_{\rm sc}/d\Omega$ of fibrous tissue via the fat subtraction model preformed on the composites. All results were applied to (i) chicken via μ-breast, (ii) chicken via μ-expt and (iii) beef via μ-breast.

breast, (ii) μ-expt and (iii) beef via μ-breast. An apparent trend can be seen in some of the curves as if the data points are more widely distributed with an increase in x. However, the size of the error bars as x increases deems this observation unreliable. The 32 data points corresponded to 31 degrees of freedom. As discussed in Section 3.4 if the calculated t-value was greater than $t_c = 2.040$ the null hypothesis could be rejected with a 95% confidence level. The t-values for $\Delta_{\rm mix}$ of chicken were 1.47 and 1.05 for calculations via μ-breast and μ-expt respectively. Beef had a t-value of 1.14. None of the calculated values were greater than t_c, therefore, the null hypothesis was retained. Similarly, for $\Delta_{\rm fib}$ the null hypothesis failed to be rejected with t-values of

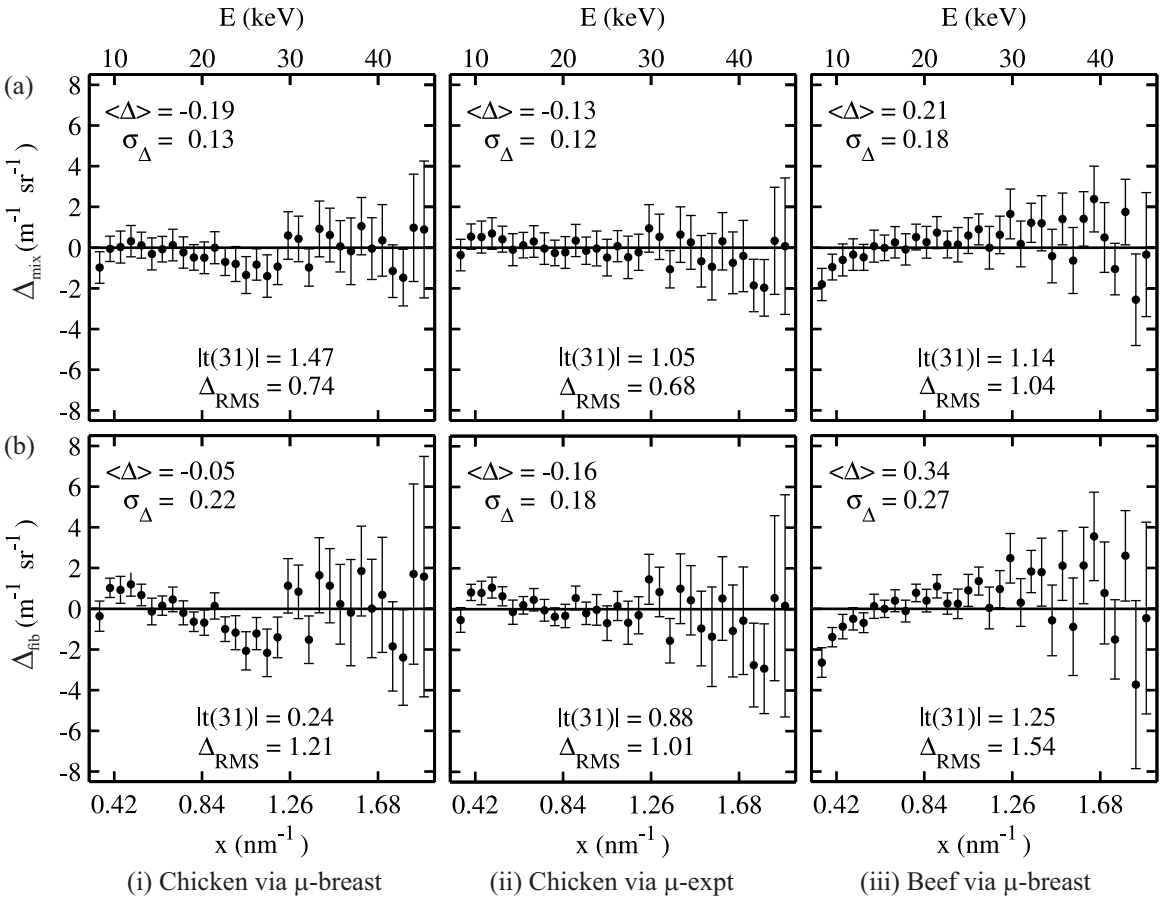

Figure 4.5: (a) Δ_{mix} and (b) Δ_{fib} for (i,ii) chicken and (iii) beef. $< \Delta >$ is the mean value, σ is the standard deviation, $|\text{t}(31)|$ is the calculated t-value for 31 degrees of freedom and Δ_{RMS} is the root mean square. Again (i) and (ii) are chicken via μ-breast and μ-expt respectively and (iii) is beef via μ-breast.

0.24(μ-breast) and 0.88(μ-expt) for chicken and 1.25(μ-breast) for the beef. Overall, the results signified that the data did not deviate from the expected mean of 0 in a statistically significant way, further verifying that the models preformed well.

Δ_{mix} had RMS results of 0.74, 0.68 for the chicken via μ-breast and μ-expt as well as 1.04 for the beef via μ-breast. Δ_{fib} had RMS results of 1.21(μ-breast) and 1.01(μ-expt) for the chicken and 1.54(μ-breast) for beef. The use of measured μ values yielded smaller RMS which would be indicative of smaller fluctuations.

4.2 Analysis With 80 kV and Various θ

This section will describe the results obtained with the modified diffractometer system which was described in Section 3.5. The first sub-section will deal with measurements done at 6° whereas the second one at 2°, 8°, 12° and 16°. Raw spectra, incident spectra, $d\mu_{\text{s}}/d\Omega$ estimates and analysis of the effectiveness of the beam stopper will be presented.

4.2.1 $\theta = 6°$

Significant efforts were made to include a beam stopper. Its' effects on the resultant $d\mu_{\text{s}}/d\Omega$ curves was of particular interest. The following results employed the use of the lead holder, brass addition and beam stopper described in Section 3.5. Figures 4.6(i) (a) and (b) show the background, $N_b(E)$, spectra obtained at $\theta = 6°$

respectively without and with the beam stopper inside the primary beam. When the beam stopper is in position the background was lower. The ratio of $\sum N_b^{WB} / \sum N_b^{NB}$ is 0.81, where NB and WB denote 'no beam stopper' and 'with beam stopper', respectively. The ratios of $N_b(E)$ with the beam stopper to that without the beam stopper are given in Fig. 4.6(i)(c). The error was calculated by propagation of error. In the range $x < 2.53$ nm^{-1} the use of the beam stopper minimized the background by an average factor of 0.27. The beamstopper seemed to have minimized the scatter from air that occurred post sample position.

The background when a sample of thickness d was in place was estimated via

$$N_{ba}(E) = N_b(E)e^{-\mu(E)d} \tag{4.1}$$

where μ is the linear attenuation coefficient of the sample. Figure 4.6(i)(a) and (b) also show the $N_{ba}(E)$ spectra obtained via attenuation by a 3 mm thick sample of polycarbonate.

The $N_s(E, \theta = 6°)$ spectrum of 3 mm PMMA is shown in Fig. 4.6(ii) (a) without and (b) with the beam stopper. Due to the use of a higher kV beam a detector response function was applied. The detector response function, developed for a CZT detector [31], was modified to correct for hole tailing and fluorescence escape for CdTe. In this section 'NR' and 'WR' stand for 'No Response' and 'With Response', respectively. All quantitative results are NR unless stated otherwise. The effects of applying the detector response are visible in Figure 4.6(ii)(a,b) as some of the low

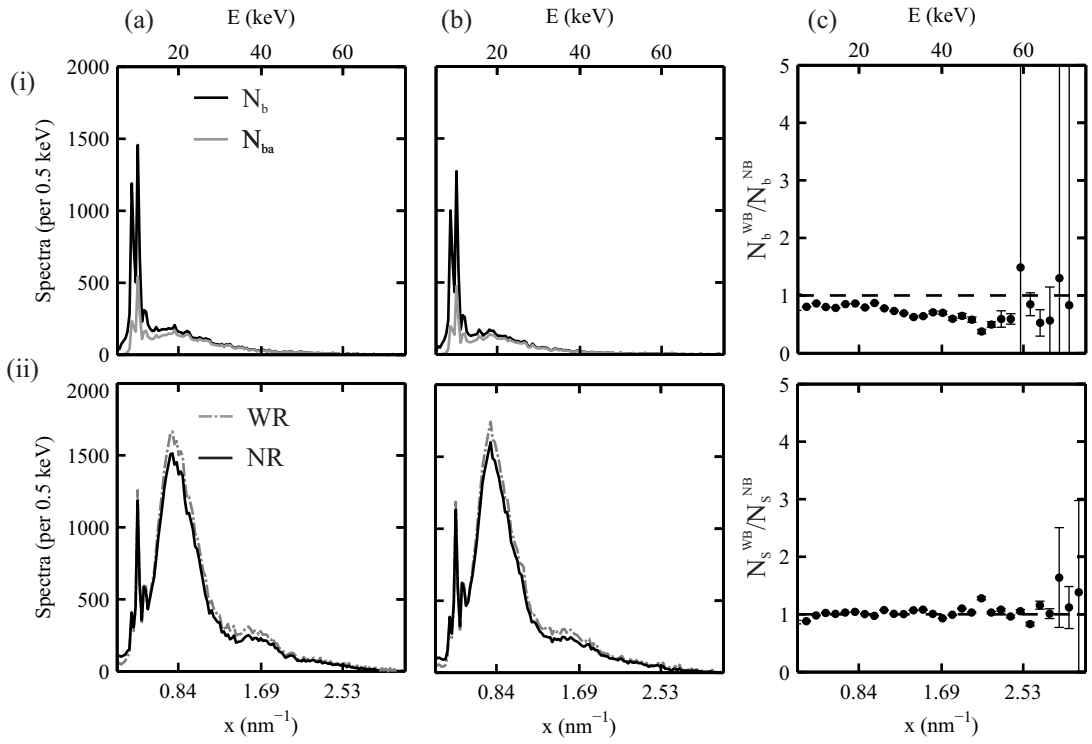

Figure 4.6: Measured spectra obtained at $\theta = 6°$ where (i) is the background and (ii) scatter from a 3 mm thick sample of PMMA. Measurements were taken (a) without and (b) with the beam stopper. (c) Ratio of the spectrum with the beam stopper to that without the beam stopper.

energy photons, as a result of fluorescence, were re-binned to higher energies.

The use of the beam stopper did not significantly change the scatter spectrum. The ratios of $N_s(E, \theta = 6°)$ with the beam stopper to that without the beam stopper are given in Fig. 4.6(ii)(c). The ratio $\sum N_s^{WB} / \sum N_s^{NB}$ for PMMA was 1.02 and for x < 2.53 nm^{-1} the signal was increased by an average factor 1.02. Although the background was reduced by the use of the beam stopper the results suggest it became a secondary source of scatter since the results with and without the beam stopper were comparable for N_s. Scattered photons from the sample may have interacted with the

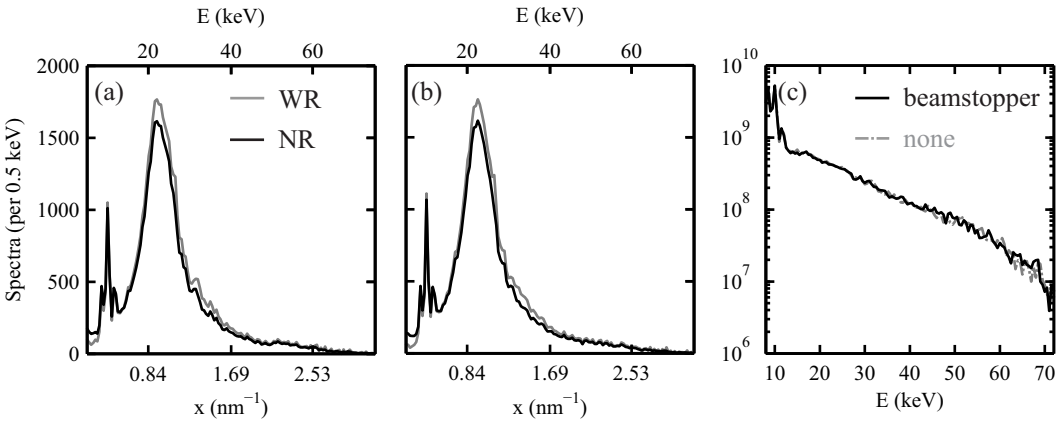

Figure 4.7: Scatter spectra obtained at 6° (a) without and (b) with the beam stopper from a 3 mm thick sample of polycarbonate. (c) Incident spectra obtained using polycarbonate with and without the beam stopper.

beam stopper which contaminated the signal.

Equation 3.1 was rearranged to obtain the incident spectrum, $N_0(E)$, via the polycarbonate scatter spectra shown in Figure 4.7(a) and (b). The $N_0(E)$ with and without the beam stopper are shown in Fig. 4.7(c). There are very little differences between the two incident spectra.

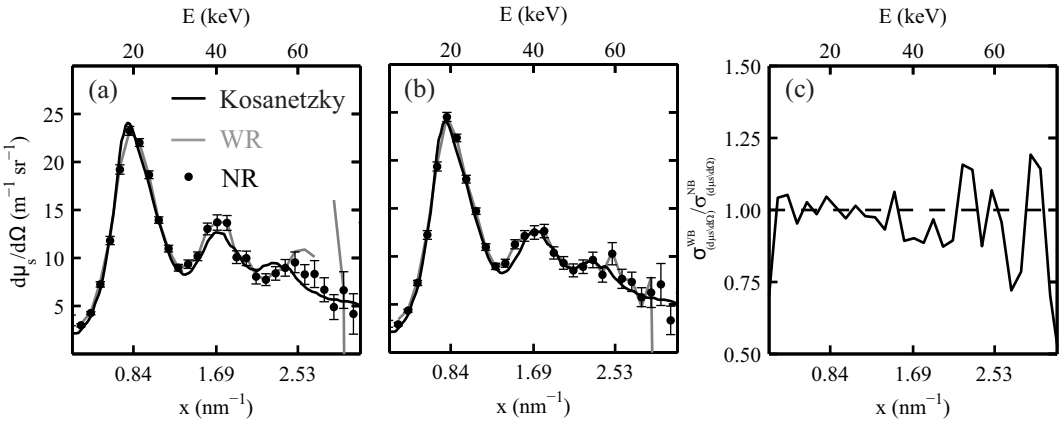

Figure 4.8: $d\mu_s/d\Omega$ of PMMA obtained at 6° (a) without and (b) with beam stopper. (c) A ratio of $\sigma(d\mu_s/d\Omega)$ with beam stopper to that without.

Figure 4.8 shows the resultant $d\mu_s/d\Omega$ (a) without and (b) with the beam stopper. The scattering coefficient matched well with literature over the entire range of x. $d\mu_s/d\Omega$ with the response function applied followed the uncorrected data points suggesting the response function may not be necessary for the analysis with 80 kV beams. A ratio of the error at each data point of $d\mu_s/d\Omega$ with the beam stopper, $\sigma^{\mathrm{WB}}_{(\mathrm{d}\mu_s/\mathrm{d}\Omega)}$, to that without, $\sigma^{\mathrm{NB}}_{(\mathrm{d}\mu_s/\mathrm{d}\Omega)}$, is given in Figure 4.8(c). The use of the beam stopper decreased the error by an average factor of 0.05 over the range of x. The remaining measurements discussed in this section employ the use of the beam stopper.

Next measurements were taken which would test the sensitivity of the incident spectrum estimation. Figure 4.9 shows the scatter spectra obtained from 5 mm thick samples of (a) polycarbonate, (b) PMMA and (c) water at the $\theta = 6^\circ$ orientation. The effects of applying the detector response are again visible in Figure 4.9. The incident spectra obtained via the three samples were calculated and are shown in Fig. 4.10. Incident spectra obtained via polycarbonate and PMMA matched fairly well as compared to that obtained using a water sample. The incident spectrum obtained via water was higher than the plastics above 40 keV.

Scatter spectra from 2 mm and 4 mm thick samples of polycarbonate and PMMA were also used to determine $N_0(E)$, however, they are not shown. The water spectrum shown in Fig. 4.9(c) was used to determine its $d\mu_s/d\Omega$. Figure 4.11 shows the resultant $d\mu_s/d\Omega$ obtained via $N_0(E)$ of (a) PMMA and (b) polycarbonate with thickness of 5, 4 and 2 mm ((i)-(iii)).

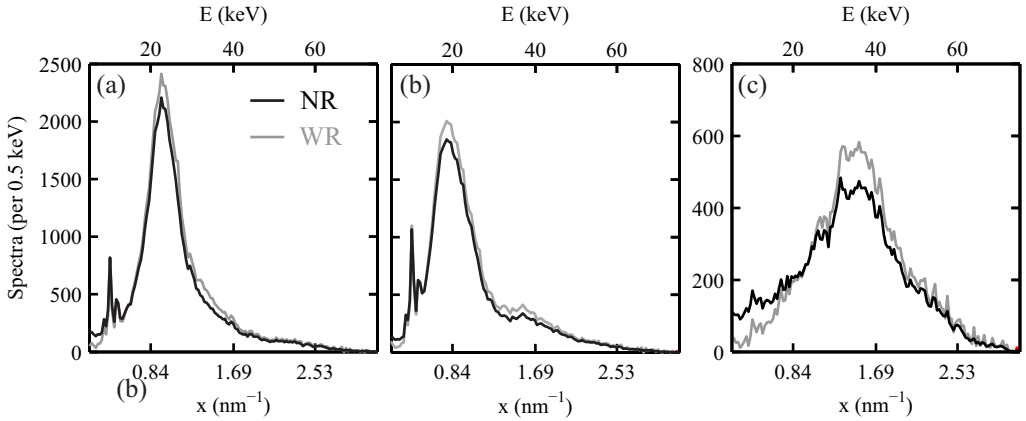

Figure 4.9: Scatter spectra obtained at 6° from 5 mm thick samples of (a) polycarbonate, (b) PMMA and (c) water.

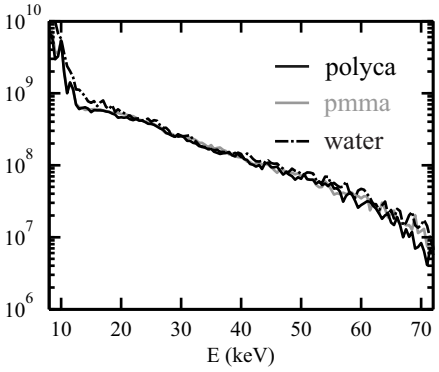

Figure 4.10: Incident spectra obtained via scatter measurements at 6° using 5 mm thick samples of polycarbonate, PMMA and water.

The measured $d\mu_s/d\Omega$ data points for H_2O matched well with literature between 0.42 nm^{-1} < x < 1.68 nm^{-1}. However, above this region discrepancies between measured and Narten's 'gold standard' were observed. The data corrected for detector response followed closely with the uncorrected data except at the limits of the $d\mu_s/d\Omega$ signals (x < 0.42 nm^{-1} and x > 2.53 nm^{-1}). Therefore, deviations from the gold standard were not a detector response issue.

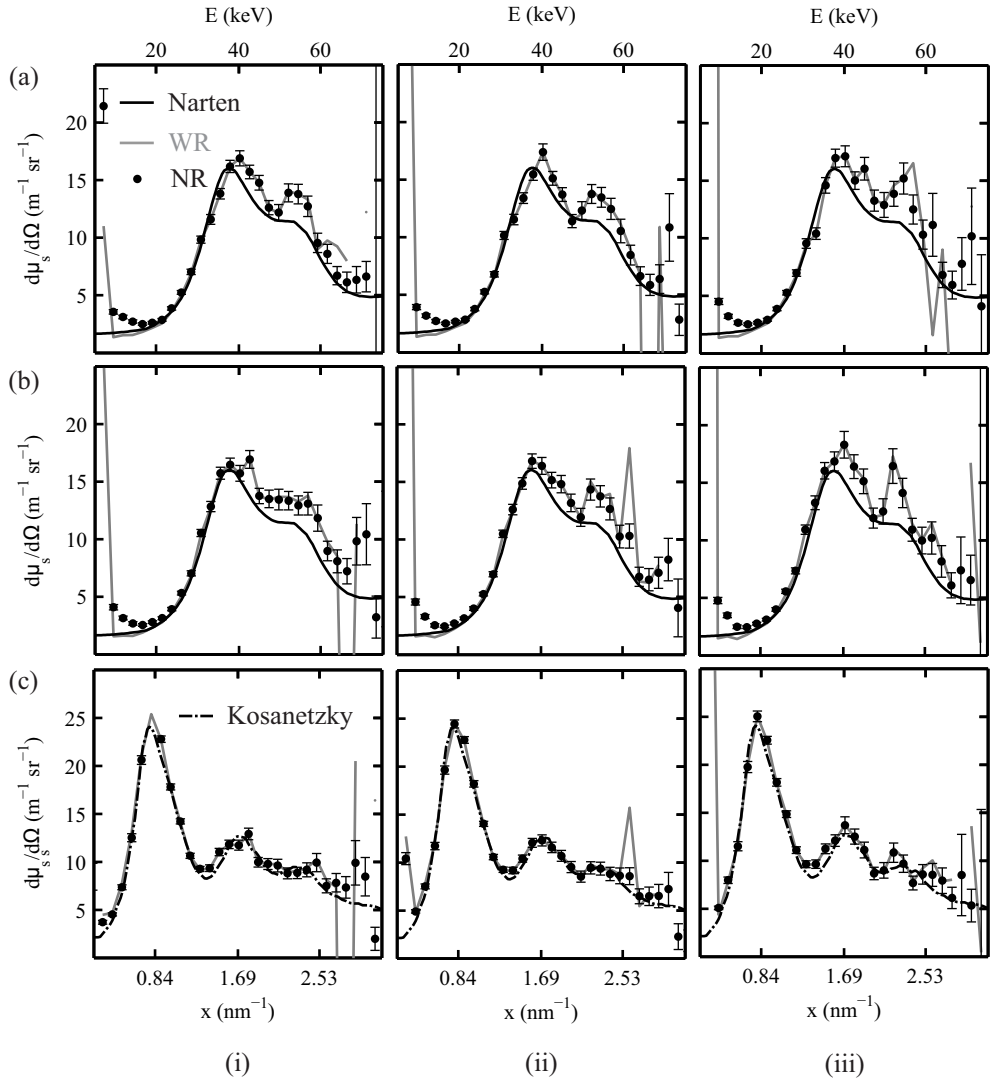

Figure 4.11: $d\mu_s/d\Omega$ at $\theta = 6°$ for 5 mm water via $N_0(E)$ (a) PMMA and (b) polycarbonate. (c) $d\mu_s/d\Omega$ at $\theta = 6°$ for 5 mm PMMA via $N_0(E)$ polycarbonate. Sample thicknesses were (i) 5 mm, (ii) 4 mm and (iii) 2 mm for the estimations of $N_0(E)$.

Figure 4.11(c) shows the same procedure using polycarbonate for $N_0(E)$ to obtain the $d\mu_s/d\Omega$ of PMMA. The resultant signals matched very well over the entire x-range and no significant differences were observed based on the thickness of plastic used to get $N_0(E)$. Again the detector response had negligible effects except at the outer x limits. Overall the use of varying sample thickness did not significantly affect the resultant $d\mu_s/d\Omega$, however, the error in the data points does increase due to the decreased number of scatter photons for thinner samples.

Consider the scatter spectra of the 5 mm thick samples of polycarbonate and water shown in Fig. 4.9(a) and (c). The $d\mu_s/d\Omega$ of polycarbonate shown in Figure 4.12(a) was obtained by using the water scatter spectrum to estimate $N_0(E)$. Due to the dependence on literature values of $d\mu_s/d\Omega$ to obtain $N_0(E)$ any potential discrepancies between the sources (polycarbonate versus water) could be a cause for some deviations. To highlight these potential differences the scattering coefficient of polycarbonate, labeled $(d\mu_s/d\Omega)$(polycn) obtained via water as discussed, was used in place of literature to obtain $N_0(E)$. The resultant $d\mu_s/d\Omega$ of PMMA using $(d\mu_s/d\Omega)$(polycn) is shown in Figure 4.12(b). Previously, when polycarbonate was used to obtained $N_0(E)$ for PMMA the results matched fairly well, however, now there is an underestimation of the coefficient in the region surrounding x = 0.84 nm^{-1}. It is interesting to note that when the detector response is applied there seems to be a better agreement in this region with literature when using the new coefficient.

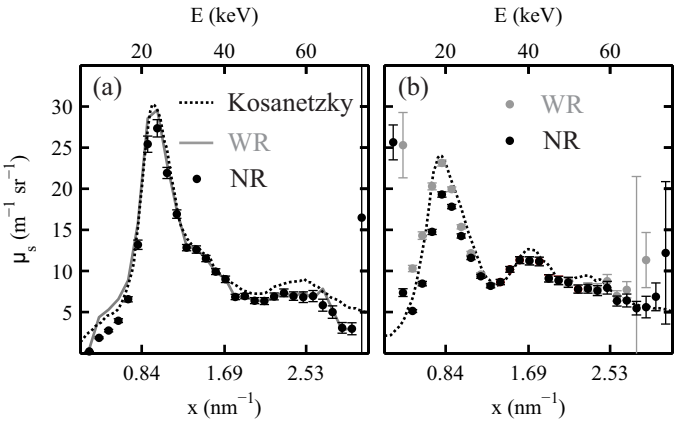

Figure 4.12: $d\mu_s/d\Omega$ of 5 mm polycarbonate at $\theta = 6°$ using the Pb holder, brass addition, beam stopper and $N_0(E)$ via 5 mm thick water. (b)$d\mu_s/d\Omega$ of 5 mm PMMA at $\theta = 6°$ using polycarbonate for $N_0(E)$ for which $d\mu_s/d\Omega$ in (a) was used.

4.2.2 $\theta = 2°$, $8°$, $12°$ and $16°$

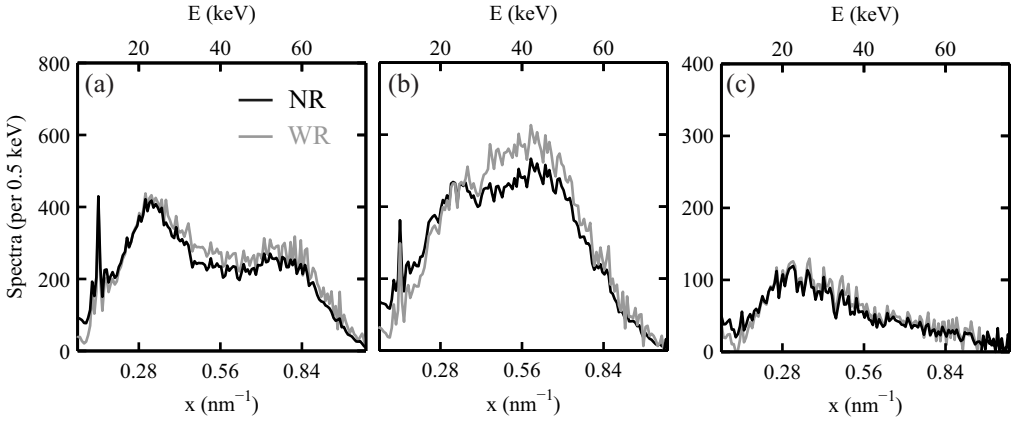

Figure 4.13: Scatter spectra obtained at 2° from 5 mm thick samples of (a) polycarbonate, (b) PMMA and (c) water.

Scatter spectra of 5 mm thick polycarbonate, PMMA and water were measured at 2° and are shown in Figure 4.13. Similarities to the 6° results were observed. The response function corrected for fluorescence photons by re-binning them to higher energies. The background and calculated incident spectra are shown in Figure 4.14.

Larger discrepancies between the calculated incident spectra were dependent on the sample used and the two plastic samples followed more closely than the water. As could be seen from Figure 3.9 the amount of scatter that occurred for water at lower angles was expected to be much smaller than that of PMMA and polycarbonate. The potential for contamination from secondary scatter could be a reason for the larger estimated incident spectra when plastics are used.

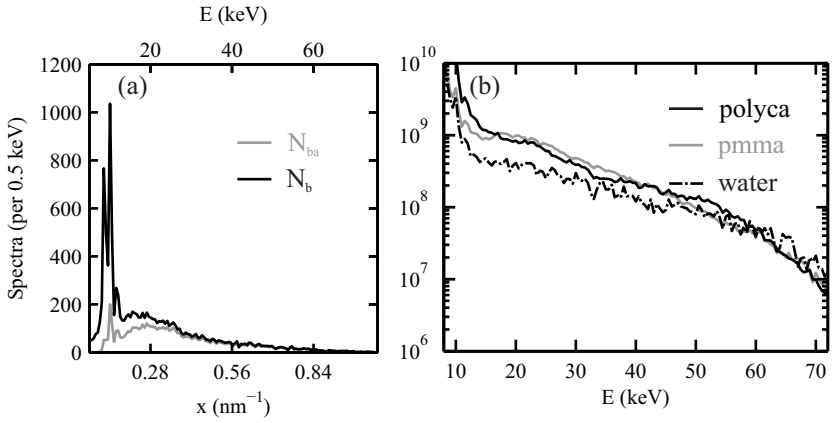

Figure 4.14: (a) Measured background spectrum, $N_b(E,\theta)$, attenuated by a 5 mm thick sample of polycarbonate, $N_{ba}(E,\theta)$ at $\theta = 2°$. (b) Incident spectra via polycarbonate, PMMA and water using 5 mm thick samples.

Consider now the scatter signals from a 3 mm thick polycarbonate sample taken at 2° and 6°. The incident spectrum obtained via the rearrangement of Eqn. 3.1 is shown in Figure 4.15(a)(i) along with that via a 5 mm thick sample (ii). It can be seen that there is a discrepancy depending on whether 2° or 6° was used. At 2° any scatter contamination from post sample would be more pronounced. Figure 4.15(b) and (c) show the resultant $d\mu_s/d\Omega$ of PMMA where the incident spectrum was taken from 6° or 2°, respectively, with the same sample thickness. In the former case the

curve grossly over estimates the scatter coefficient. When the incident spectrum was obtained via the 2° $N_s(E, \theta = 2°)$, the results are better, however, disagreement from literature occurred for x > 0.6 nm^{-1}.

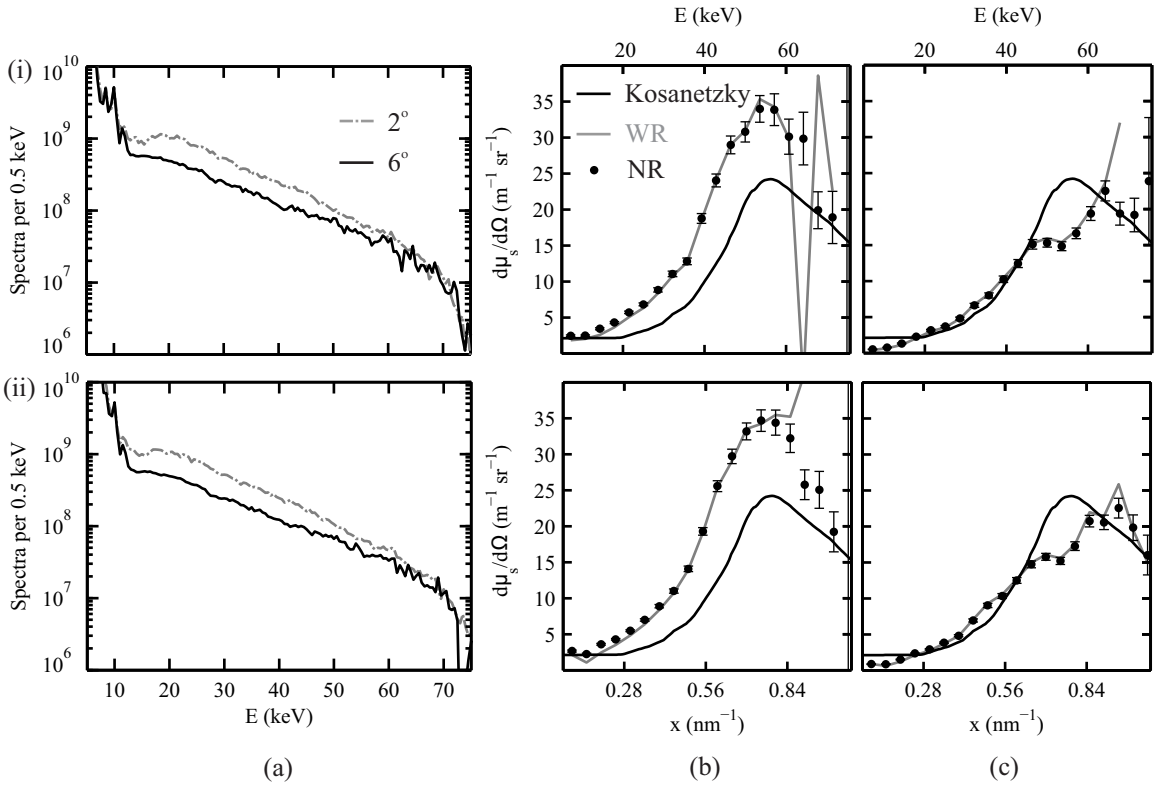

Figure 4.15: (a) $N_0(E)$ obtained at 2° and 6° using polycarbonate. $d\mu_s/d\Omega$ of PMMA obtained via 2° scatter and $N_0(E)$ from (b) 6° and (c) 2°. Sample thicknesses were (i) 3 mm and (ii) 5 mm.

Now consider $N_s(E, \theta)$ of 3 mm thick PMMA obtained at θ = 8°, 12° and 16°. The scatter was used to compare any potential differences in the estimated $N_0(E)$. A 4.2 mm Pb aperture was used at the sample as described in Section 3.5 as well as the appropriate beam stopper depending on the angle. The brass addition was removed from the system and a 3.3 mm aperture was used at the detector. Figure 4.16(a)

shows the scatter spectra from a 3 mm thick sample of PMMA and (b) the N_b and N_{ba} spectra for θ = (i) 8°, (ii) 12° and (iii) 16°. As anticipated the background decreased as θ increased. The increase in sample scatter for the 12° measurement is due to the higher probability of scatter at low energy for PMMA as was shown in Figure 3.9.

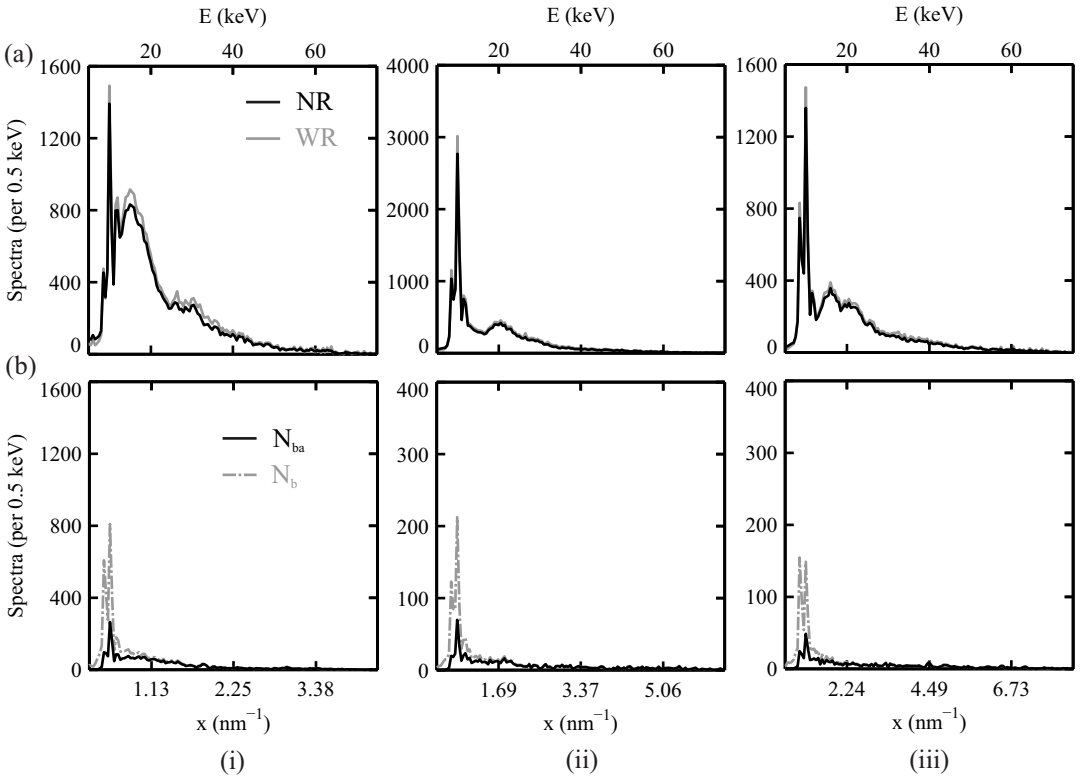

Figure 4.16: (a) 3 mm thick sample of PMMA N_s and (b) N_b and N_{ba} spectra obtained at (i) 8°, (ii) 12° and (iii) 16°.

Figure 4.17 shows the calculated $N_0(E)$ using the scatter spectra from Figure 4.16. There appears to be a fairly good match but the 12° and 16° $N_0(E)$ follow closely with the 8° spectra deviating most. This indicates that some scatter contamination is occurring which is highlighted when the difference between angles is larger.

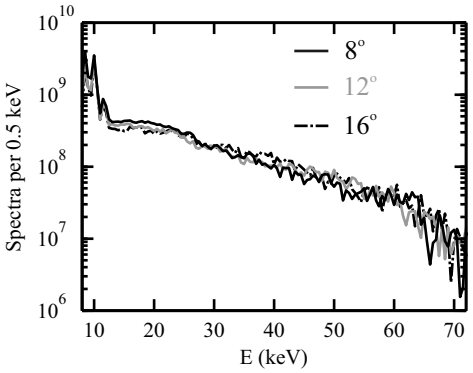

Figure 4.17: Estimated incident spectra obtained at 8°, 12° and 16° using 3 mm thick PMMA.

Figure 4.18 shows the $d\mu_s/d\Omega$ of PMMA obtained using the three incident spectra. The scatter measurement to obtain $d\mu_s/d\Omega$ of PMMA was done at $\theta = 6°$ with a 3 mm thick sample. As the angle used for $N_0(E)$ increases a disagreement from literature becomes more prominent especially in the region 0.42 nm^{-1} < x < 1.27 nm^{-1}. The results suggest that there is some contamination, such as secondary scatter, at lower angles which is increasing the number of photons which interact with the detector. When the incident spectrum and scatter spectrum are obtained using an $N_s(E, \theta)$ from similar angles ($\theta_i \approx \theta_s$) the problem is minimized.

The effectiveness of the beam stopper for $\theta = 2°$ measurements was tested using the same system step up mentioned above. Figure 4.19 shows the step by step analysis. Figure 4.19 (i) shows the background spectra, (ii) scatter spectra from 5 mm PMMA and (iii) its' $d\mu_s/d\Omega$; (a) without beam stopper, (b) with the beam stopper; (c) is a ratio of with over without beam stopper for (i) and (ii). Figure 4.19(c)(iii) shows the ratio of the error in $d\mu_s/d\Omega$ with over without the beam stopper. A poly-

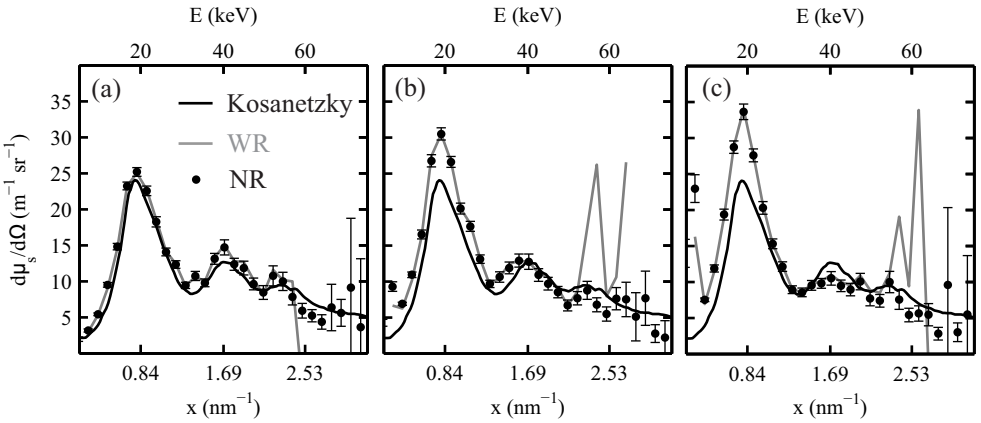

Figure 4.18: $d\mu_s/d\Omega$ of PMMA obtained via a scatter measurement at $\theta = 6°$ with a 3 mm thick sample. $N_0(E)$ was obtained using a 3 mm polycarbonate sample at (a) 8°, (b) 12° and (c) 16°.

carbonate sample 5 mm thick was used to obtained $N_0(E)$ via a scatter measurement done at $\theta = 2°$.

As seen previously the beam stopper decreases the background. The ratio of $\sum N_b^{WB} / \sum N_b^{NB}$ is 0.08 and the signal was decreased by an average factor of 0.83. The effects of the beam stopper on the background made the most significant difference at low angles. $\sum N_s^{WB} / \sum N_s^{NB}$ is 1.01 and the scatter signal remains the same on average. Again the results suggest that although the beam stopper decreased the background it may have increased the scatter signal.

The $d\mu_s/d\Omega$ results followed fairly close together; with the analysis deviating from literature for 0.65 nm^{-1} < x < 0.9 nm^{-1}. The same deviation was seen using the other system set up. The uncertainty in $d\mu_s/d\Omega$ obtained with the beam stopper (i.e. $\sigma^{WB}_{(d\mu_s/d\Omega)}$) was reduced by a factor of 0.23 in the region 0.1 nm^{-1} < x < 1.05 nm^{-1} as compared to the no beam stopper case.

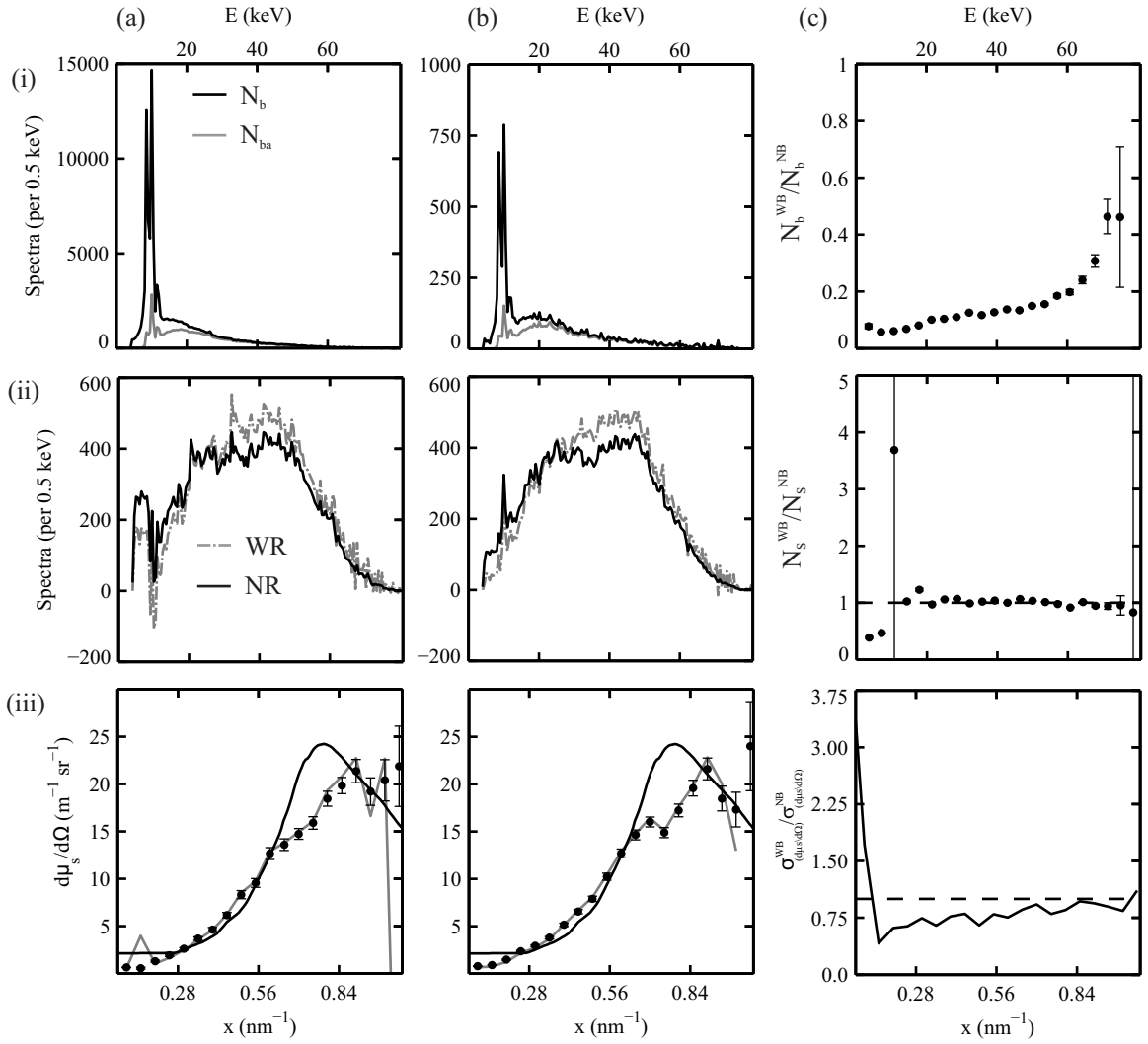

Figure 4.19: Beam stopper analysis at 2°. (i) Background spectra, (ii) scatter spectra of 5 mm thick PMMA and (iii) its' $d\mu_s/d\Omega$: (a) without and (b) with beam stopper. (c) The ratio of (i) background, (ii) scatter and $\sigma(d\mu_s/d\Omega)$ with beam stopper to that without.

Chapter 5

Discussion

In this chapter the results obtained with animal tissue will be discussed followed by the 80 kV measurements.

5.1 Animal Tissue

The WAXS fat subtraction analysis obtained with animal tissue were encouraging, although some improvements will be incorporated in the future. The measurements of μ and the sample preparation (especially its thickness) will be optimized since they need to be known accurately. The purity of our base-line pure samples will be quantified via combined μ and image analysis. Namely, μ values determined for a 25 μm diameter column of the tissue sample will be measured. The sample will then be imaged and its fat content will be estimated using the measured μ. For a pure sample of fat, ν_{fat} should be equal to 1 whereas $\nu_{\text{fat}} = 0$ for a pure fibrous sample.

Ideally, if true μ and $d\mu_s/d\Omega$ values could be obtained for pure tissue, then the need for a separate system to estimate the fat content within a biopsy could potentially be omitted. Namely, Eqn. 3.1 may be rearranged to solve for $\overline{\nu}_{\text{fat}}$ using singular value decomposition.

Another necessity in validation of the applied WAXS protocols would require a larger $d\mu_s/d\Omega$ population for checking reproducibility of measurements. The timing between tissue removal from formalin solution, imaging, μ-expt and scatter measurements needs to be monitored. As discussed in Section 4.1.3 the models appeared to perform better with the use of measured μ values, however, the only comparison is that of the chicken $d\mu_s/d\Omega$. The beef had to be omitted due to the preparation procedure being delayed. A more efficient preparation procedure would ensure accurate measurements of larger numbers of $d\mu_s/d\Omega$s.

5.2 80kV and θ Analyses

The optimization of the WAXS system to allow for a wider x-range was encouraging. Modifications which were done to include a beam stopper were informative. Its' use at 6° decreased the background by a factor of 0.27. However, simulation from Section 3.5 estimated a decrease in the back ground of a factor of 0.5. An increase by a factor of 1.01 was observed in the scatter spectrum when a sample was in place, suggesting that the beam stopper introduces a secondary source of scatter. To address this problem efforts should be made into a different method of reducing the

post sample scatter (e.g. air scatter). A possible solution would be to use multiple apertures that reduce the field of view of the detector. This approach was attempted through the use of the brass addition, however, a more robust set up is necessary.

Results using polycarbonate and PMMA at different thickness to obtain $N_0(E)$ were good. $d\mu_s/d\Omega$ of polycarbonate and PMMA matched well to literature over the entire x-range obtained at 80 kV for $\theta = 6°$. The results for water did not match as well, however, they were still fairly close to the gold standard. No significant effects were observed when using different sample thicknesses to obtain the incident spectrum. Both plastic and water results show that the application of the response function may not be necessary for 80 kV.

The results obtained when using angles other than $\theta = 6°$ were less ideal. The discrepancies appear to arise from the source of $N_0(E)$. As seen in Figure 4.15 the estimated incident spectra vary when the angles used are different. Disagreements are highlighted when the angle from which $N_0(E)$ is obtained differs from that of $N_s(E, \theta)$. Disagreement was present for the $\theta = 2°$ analysis even if $N_0(E)$ was obtained with the same orientation. Therefore, an effort to determine $N_0(E)$ via methods other than scatter could be attempted by building a shielding case for the detector which would include a small aperture such that a small portion of the incident beam could be sampled in the $\theta = 0°$ orientation. The ability to measure $N_0(E)$ directly eliminates the need for literature values for its' determination.

Chapter 6

Conclusion

The fat subtraction protocol was successfully outlined in this work. First, the measurement of scatter signals from a sample biopsy ROI were obtained using a custom built diffractometer cabinet. Second, a projection imaging system was used to determine information about the composition of the biopsy. Finally, models to extract the differential linear scattering coefficients, μ_s, of fatless tissue within the ROI were applied. The protocol was described in detail in Chapter 3. The model described a method to subtract a known fractional volume of fat from a (composite) biopsy ROI given knowledge of μ_s of the components. Simulations were able to show that knowledge of the fractional volume of fat within the ROI was sufficient.

The protocol was preformed on animal tissue phantoms since they mimic breast tissue. Known μ_s signals of pure fat and fibrous tissue were obtained for comparison. Results showed that subtraction of fat content from composite tissue samples matched well with those of the pure samples. The protocol was, therefore, validated.

The WAXS signals of the animal tissue were obtained using a 50 kV beam and scatter angle of 6°. Preliminary work was done to expand the momentum transfer range by modifying the cabinet to accommodate measurements done between 2° and 16° at 80 kV. Expanding this range could potentially allow for more information to be extracted a sample. The results obtained at 6° and 80 kV using water, PMMA and polycarbonate with this new set up were promising.

The preliminary methods presented in this work are currently under investigation and it is not possible to specify their potential in the clinical setting. The goal of devising a system which allowed the comparison of WAXS signals of cancer and fibroglandular tissue without the effects of fat has been successful within the small data set of animal tissue shown. The ability to distinguish between the WAXS signals of fibroglandular and cancerous tissue still needs to be researched and will be the determining factor of the methods' viability in the clinical setting. Once the methods are proven reproducible using a large sample set of animal tissue breast tissue biopsies analysis will be required. If the above is successful there is potential for a complementary method of diagnosis to histology.

Appendix A

Formalin

Formalin is a commonly used aldehyde based tissue fixative derived from formaldehyde. A detailed account of the interactions of formaldehyde (formalin) with tissues described by Kiernan. [22] Formaldehyde gas is dissolved in water to form methylene hydrate. The chemical reaction is shown in Fig. A.1 (a). These molecules react together creating polymer chains. To prevent the polymers from developing into long chains methanol is introduced into the solution. These higher order polymers are insoluble and form a dangerous white powder called para formaldehyde. Therefore, formalin is created using formaldehyde, methanol and water. A 10 % formalin solution which contains 4 % formaldehyde will contain 1% methanol.

Formaldehyde will react with one or two proteins [Fig. A.1 (b) or (c)] within a tissue depending on the proximity. If the formaldehyde interacts with only one protein a hydroxy-methylene compound becomes attached to the reacting protein.

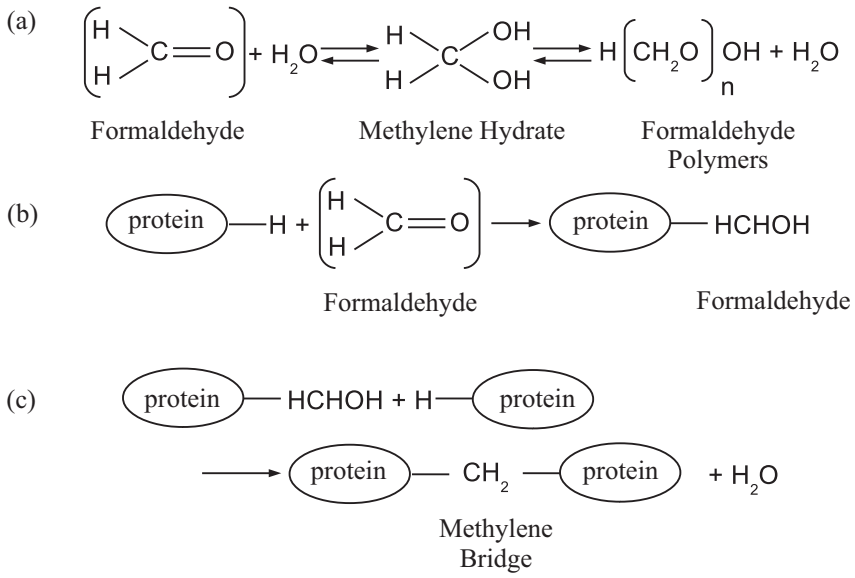

Figure A.1: Formaldehyde interaction with (a) water, (b) a signal protein and (c) two proteins. [22]

If there is another protein within close proximity then the two proteins will become attached by a methylene bridge and a water molecule will be released. However, the two protein interaction requires much more time than the single protein interaction.

To study the effects that formalin has on the WAXS signals of tissue attempts to use fresh tissue were made. Fresh-frozen tissue (via nitrogen) was obtained and comparative WAXS results were presented in a poster at CARO/COMP 2013. Fresh tissue was much harder to handle and the use of formalin was deemed the most effective way of validating the WAXS fat subtraction protocol.

Appendix B

The Definition of Absorbed Dose and Exposure

The work described in previous chapters was concerned with biopsies and as such the biological effects of ionizing radiation were not inherently a problem which needed to be addressed. However, two important quantities will be defined; absorbed dose and exposure.

Absorbed dose or Dose (D) is quantity which is directly related to the effects of ionizing radiation on a patient. It is defined as the energy absorbed by a unit mass of material given by;

$$D = \frac{d\overline{E_{ab}}}{dm} \tag{B.1}$$

The SI unit for dose is the gray (Gy) where 1 Gy = 1 J/kg. The historical unit for dose was radiation absorbed dose (rad) where 1 rad = 100 ergs/g = 10^2 J/kg.

Exposure quantifies the interaction of x-rays with air. It is defined by the ICRU as

$$X = \frac{dQ}{dm} \tag{B.2}$$

where dQ is the absolute value of the total charge of the ions of one sign produced in air when all of the electrons liberated by photons in air of mass dm are stopped completely in air. [18] In other words it is a quantity which describes the ionization produced in air by photons. The units of exposure are coulombs per kg. The original unit of exposure was the Roentgen given by 1 C/kg = 3876 R.

The calculation of absorbed dose from exposure is not easily accomplished in real world conditions. It is only possible under electron equilibrium which is defined as the condition in which the same number of electrons enter and exit a volume while maintaining the same energy distribution. As discussed in Section 2.2 x-ray interactions with matter are quite complex. The ability for electronic equilibrium to be maintained is not ideal since attenuation will occur in the medium. [20] Other methods to determine the absorbed dose such as simulations may be preformed, however, this was not the focus of this work.

Appendix C

Linear Differential Scattering Cross Section

The definition of cross section in physics is the probability that a scattering event will occur within an area when an incident beam interacts with a material. The concept may be simplified to the length traveled in the material referred to as the linear cross section. Consider photons incident on a material along an axis. If a number of photons, N_s are scattered along a distance traveled Δx the total linear scattering cross section may be expressed mathematically as

$$\sigma_s = \frac{N_s}{N}\frac{1}{\Delta x} \tag{C.1}$$

where N is the incident number of photons. When the angle of scatter is considered the concept can be further simplified as the fractional number of photons scattered, ΔN_s, into an angle θ. The differential linear scattering cross section may be defined by

$$\frac{d\mu_s}{d\Omega} = \frac{\Delta N_s}{N}\frac{1}{\Delta x} \tag{C.2}$$

where $d\Omega$ is the differential solid angle (Ω). The quantity describes the probably of a photon scattering into a solid angle $d\Omega$ per unit length in a scattering material.

Figure C.1 (a) shows a schematic of a photon scattering at angle θ over a length Δx. The photon is scattered into an area on a sphere between θ and $d\theta$. Figure C.1 (b) illustrates the concept of the solid angle. dA may be thought of as the area a cone cuts out of a sphere. dΩ is a 2D interpretation of an angle in 3D space. For $d\theta \ll \theta$ it can be shown that $d\Omega$=2πsinθdθ. [18]

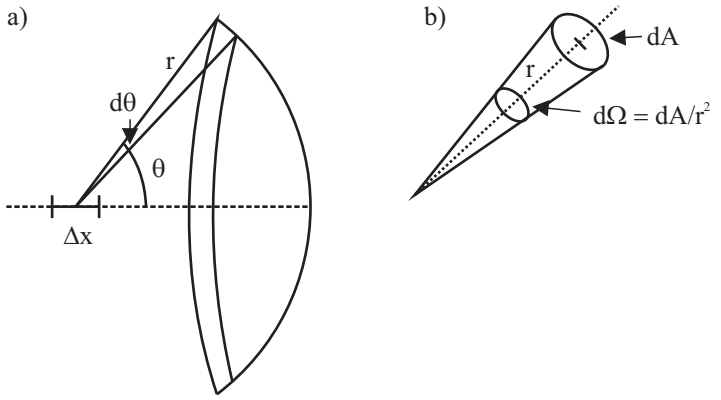

Figure C.1: (a)Schematic of photon scattering into dΩ. (b) Concept of the solid angle.

Bibliography

[1] H. Abramczyk, J. Surmacki, B. Broek-Puska, Z. Morawiec, and M. Tazbir. The hallmarks of breast cancer by raman spectroscopy. *J. Mol. Struc.*, 924, 2009.

[2] M.E. Poletti A.L.C. Conceicao, M. Antoniassi. Preliminary study of human breast tissue using synchrotron radiation combining waxs and saxs techniques. *Appl. Radiat. Isotopes*, 68:799–803, 2010.

[3] Amptek. Charge trapping in xr-100t-cdte cadmium telluride detectors application note. 2007.

[4] J.A. Gardecki J. Nazemi R. Shenk N. Wang R.R. Dasari M. Fitzmaurice M.S. Feld A.S Haka, Z. Volynskaya. Diagnosing breast cancer using raman spectroscopy: prospective analysis.

[5] M. Fitzmaurice J. Crowe R.R. Dasari M.S. Feld A.S. Haka, K.E. Shafer-Peltier. Diagnosing breast cancer by using raman spectroscopy. *Proc Natl Acad Sci*, 102, 2005.

[6] J.M. Boone, T.R. Nelson, K.K. Lindfors, and J.A. Seibert. Dedicated breast ct: Radiation dose and image quality evaluation.

[7] N.F. Boyd, H. Guo, L.J. Martin, L. Sun, J. Stone, E. Fishell, R.A. Jong, G. Hislop, A. Chiarelli, S. Minkin, and M.J. Yaffe. Mammographic density and the risk and detection of breast cancer. *N. Engl. J. Med.*, 356:227–236, 2007.

[8] M.J. Anjos R.T. Lopes D. Braz C.R.F. Castro, R.C. Barroso. Coherent scattering characteristics of normal and pathological breast human tissues. *Radiation Physics and Chemistry*, 71:649–651, 2004.

[9] D. M. Cunha, O. R. Oliveira, C. A. Perez, and M. E. Poletti. X-ray scattering profiles of some normal and malignant human breast tissues. *X-Ray Spectrom.*, 35:370–374, 2006.

[10] K.Verghese D.E. Peplow. Measured molecular coherent scattering form factors of animal tissues, plastics and human breast tissue. *Phys. Med. Biol*, 43:2431–2452, 1998.

[11] M.J. Farquharson, A. Al-Ebraheem, S. Cornacchi, G. Gohla, and P. Lovrics. The use of x-ray interaction data to differentiate malignant from normal breast tissue at surgical margins and biopsy analysis. *X-Ray Spectrom*, 42:349–358, 2013.

[12] K. Geraki, M.J. Farquharson, and D.A Bradley. *American College of Radiology: Breast Imaging Reporting and Data System (BIRADS). Reston, VA: American College of Radiology*, 1993.

[13] K. Geraki, M.J. Farquharson, and D.A Bradley. X-ray fluorescence and energy dispersive x-ray diffraction for the quantification of elemental concentrations in breast tissue. *Spectroscopy*, 49:99–110, 2004.

[14] J.A. Griffiths, G.J. Royle, A.M. Hanby, J.A. Horrocks, S.E. Bohndiek, and R.D. Speller. Correlation of energy dispersive diffraction signatures and microct of small breast tissue samples with pathological analysis. *Phys. Med. Biol.*, 52:6151–6164, 2007.

[15] J.A. Harvey and V.E. Bovbjerg. Quantitative assessment of mammographic breast density: relationship with breast cancer risk. *Radiology*, 230:29–41, 2004.

[16] H. Hubbell, Wm. J. Veigele, E. A. Briggs, R. T. Brown, D. T. Cromer, and R. J. Howerton. Atomic form factors, incoherent scattering functions, and photon scattering cross sections. *J. Phys. Chem. Ref. Data*, 1975.

[17] ICRU. Photon, electron, proton, and neutron interaction data for body tissues,. Technical report, ICRU Report 46(ICRU, Bethesda, MD), 1992.

[18] H. E. Johns and J. R. Cunningham. *The Physics of Radiology*. Charles C. Thomas, Publisher Ltd, 4th edition, 1983.

[19] P.C. Johns and M.J. Yaffe. X-ray characterization of normal and neoplastic breast tissues. *Phys. Med. Biol.*, 32:675–695, 1987.

[20] Faiz M. Khan. *The Physics of Radiation Therapy*. Lippincott Williams Williams, 4 edition.

[21] G. Kidane, R.D. Speller, G.J. Royle, and A.M. Hanby. X ray scatter signatures for normal and neoplastic breast tissues. *Phys. Med. Biol.*, 44:1791–1802, 1999.

[22] John A. Kiernan. Formaldehyde, formalin, paraformaldehyde and glutaraldehyde: What they are and what they do. *Microscopy Today*, 00, 2000.

[23] J. Kosanetzky, B. Knoerr, G. Harding, and U. Neitzel. X-ray diffraction measurements of some plastic materials and body tissues. *Med. Phys.*, 14:526–532, 1987.

[24] Dex Kouna. Methods for measuring signals at smaller angles with a wide-angle x-ray scatter system. Master's thesis, Laurentian University, 2013.

[25] R. LeClair. Measurement of total linear attenuation coefficients of tissues using energy dispersive transmission measurements with a cdte detector. *Physics in Canada*, 63:117, 2007.

[26] R.J. LeClair, M.M. Boileau, and Y. Wang. A semianalytic model to extract differential linear scattering coefficients of breast tissue from energy dispersive x-ray diffraction measurements. *Med. Phys.*, 33:959–967, 2006.

[27] R.J. LeClair and P.C. Johns. A semianalytic model to investigate the potential applications of x-ray scatter imaging. *Med. Phys.*, 25:1008–1020, 1998.

[28] R.J. LeClair and P.C. Johns. Analysis of spectral blur effects in x-ray scatter imaging. *Med. Phys.*, 26:1811–1816, 1999.

[29] R.J. LeClair and P.C. Johns. X-ray forward-scatter imaging: Experimental validation of model. *Med. Phys.*, 28:210–219, 2001.

[30] R.J. LeClair and P.C. Johns. Optimum momentum transfer arguments for x ray forward scatter imaging. *Med. Phys.*, 29:2881–2890, 2002.

[31] R.J. LeClair, Y. Wang, P. Zhao, M. Boileau, and F. Fleurot. An analytic model for the response of a czt detector in diagnostic energy dispersive x-ray spectroscopy. *Med. Phys.*, 33:1008–1020, 2006.

[32] Valerie A. McCormack and Isabel dos Santos Silva. Breast density and parenchymal patterns as markers of breast cancer risk: a meta-analysis. *Cancer Epidemiol Biomarkers Prevention*, 15:1159–1169, 2006.

[33] L.R.M. Morin. Molecular form factors and photon coherent scattering cross sections of water. *J. Phys. Chem. Ref. Data*, 11:1091–1098, 1982.

[34] A. O'Connell, D.L. Conover, Y. Zhang, P. Seifert, W. Logan-Young, C. L. Lin, L. Sahler, and R. Ning. Cone-beam ct for breast imaging: Radiation dose, breast coverage, and image quality. *AJR*, 195:496–509, 2010.

[35] D.M. Cunha M.E. Poletti C.A. Pela O.R. Oliveira, A.L.C. Conceicao. Identification of neoplasias of breast tissues using a powder diffractometer. *Journal of Radiation Research*, 49:527–532, 2008.

[36] S.R. Peters. *A Practical Guide to Frozen Section Technique*. Springer, 1st edition, 2009.

[37] E.F. Plechaty, D.E. Cullen, and R.J. Howerton. Tables and graphs of photon interaction cross sections from 1.0kev to 100mev derived from the lll evaluated nuclear data library, ucrl-50400. Technical report, Lawrence Livermore Laboratory, 1975.

[38] M.E. Poletti, O.D. Goncalves, , and I. Mazzaro. X ray scattering from human breast tissues and breast equivalent materials. *Phys. Med. Biol.*, 47:47–63, 2002.

[39] E. A. Ryan and M. J. Farquharson. Angular dispersive x-ray scattering from breast tissue using synchrotron radiation. *Radiation Physics and Chemistry*, 71:971–972, 2004.

[40] E. A. Ryan and M. J. Farquharson. Breast tissue classification using x-ray scattering measurements and multivariate data analysis. *Phys. Med. Biol.*, 52:6679–6696, 2007.

[41] J.A. Horrocks J.L. Jones R.D. Speller S. Pani, E.J. Cook. Characterization of breast tissue using energy-dispersive x-ray diffraction computed tomography. *Appl Radiat Isot.*, 68:1980–1987, 2010.

[42] C.M. Shafer, E. Samei, and J.Y. Lo. The quantitative potential for breast tomosynthesis imaging. *Med. Phys.*, 37:1004–1016, 2010.

[43] Canadian Cancer Society. Canadian cancer statistics. 2013.

[44] R. Y. Tang, C. Laamanen, N. McDonald, and R. J. LeClair. WAXS fat subtraction model to estimate differential linear scattering coefficients of fatless breast tissue: Phantom materials evaluation. *Med. Phys.*, 41:053501(7pp.), 2014.

[45] R. Y. Tang, N. McDonald, C. Laamanen, and R. J. LeClair. A method to estimate the fractional fat volume within an ROI of a breast biopsy for WAXS applications: Animal tissue evaluation. *Med. Phys.*, 41:113501(8pp.), 2014.

[46] M.A. Oghabian V. Changizi, A.A. Kheradmand. Application of small-angle x-ray scattering for differentiation among breast tumors. *J Med Phys.*, 33:19–23, 2008.

[47] C. M. Vachon, V. S. Pankratz, C. G. Scott, S. D. Maloney, T. Milanese M. J. Carston K. Ghosh, K. R. Brandt, and T. A. Sellers. Longitudinal trends in mammographic percent density and breast cancer risk. *Cancer Epidemiol. Biomarkers Prev.*, 16:921–928, 2007.

[48] Robert S. Witte and John S. Witte. *Statistics*. J. Wiley, Chichester, 7th edition, 2003.

[49] M.M. Fekry S.M. Talaat A.A. Elsayed W.M. Elshemey, O.S. Desouky. The diagnostic capability of x-ray scattering parameters for the characterization of breast cancer. *Med. Phys.*, 37:4257–265, 2010.

[50] JN Wolfe. Breast patterns as an index of risk for developing breast cancer. *American Journal of Roentgenology*, 126:1130–1137, 1976.

[51] JN Wolfe. Risk for breast cancer development determined by mammographic parenchymal pattern. *Cancer*, 37:2486–2492, 1976.

[52] M. Yaffe. Measurement of mammographic density. *Breast Cancer Research*, 49:99–110, 2008.

[53] M. J. Yaffe, N. F. Boyd, J. W. Byng, R. A. Jong, E. Fishell, G. A. Lockwood, L. E. Little, and D. K. Tritchler. Breast cancer risk and measured mammographic density. *Cancer Epidemiol. Biomarkers Prev.*, 7:47–55, 1998.